Development of the Silicon Vertex Detector for Belle II experiment

Nobuhiro Shimizu
Aihara/Yokoyama lab.
Department of Physics, University of Tokyo
7-3-1 Hongo, Bunkyo-ku, Tokyo 113-0033 JAPAN
e-mail: shimizu@hep.phys.s.u-tokyo.ac.jp

2014/01/07

Abstract

Belle II experiment at KEK (Tsukuba, Japan) is planning to start to collect e^+e^- data from 2016 with SuperKEKB accelerator and Belle II detector, where the luminosity of the accelerator will be $80 \times 10^{34}\mathrm{cm}^{-2}\mathrm{s}^{-1}$, 40 times as large as that of the former accelerator KEKB. In order to accommodate its high luminosity, the upgrade of the detector is now ongoing.

We are responsible for the development of an outermost layer of the Si-Strip Vertex Detector (SVD). SVD is one of the Belle II subdetectors, which precisely measures position of charged particles by using Double-sided Si-Strip Detector (DSSD). The outermost layer of SVD is composed of sixteen ladders and we plan to start mass production from April 2014. It is necessary to develop a ladder assembly procedure that can accomplish alignment precision within a limited production time. For example, a B meson, which is one of the main target of Belle II, flies approximately 100 μm from interaction point. In order to achieve the vertex resolution required for the measurement of time dependent decay rate of B mesons, we set the goal of alignment precision to be 10 μm.

In order to proceed to the mass production, we developed ladder assembly procedures. We have developed support fixtures (jigs) so that everyone can fix the components of ladder. However, because the positioning precision of jigs is approximately 100 μm, we need to develop an additional alignment procedure of DSSDs.

We have successfully developed special jig and an alignment software to align DSSDs. After the assembly of the ladder, the displacement of DSSDs are measured and the information will be utilized for physics analysis.

In order to evaluate the alignment precision of DSSDs in the finished ladder, we have assembled a dummy mockup by substituting aluminum plates for the DSSDs, where we found a horizontal displacement of the DSSDs by $\sim$100 μm. We have identified several possible sources of the displacement. Further study is necessary to accomplish the required alignment precision of assembled ladders.

Contents

Chapter 1

Introduction

The Belle experiment at KEK (Tsukuba, Japan) collected 1040 fb^{-1} of data sample using e^+e^- energy-asymmetric collider KEKB. It ran from June 1999 to June 2010 and contributed to the progress of high energy physics, most notably a verification of a mechanism of $\mathcal{CP}$ violation which resulted in the Nobel prize in 2008. On the other hand, there are some possible hints of new physics which need to be confirmed with more precise measurements.

Faced with the situation, Belle II experiment is planning to start data taking with e^+e^- energy-asymmetric collider SuperKEKB from 2016. With the upgrade of accelerator, the luminosity, 80×10^{34} cm^{-2}s^{-1}, becomes 40 times as large as that of former experiment Belle. It is expected that the sign of new physics will be found with the largest statistics the world never seen. Since the upgrade of accelerator requires detector also to improve its performance, upgrade of the detector for Belle II is ongoing.

The University of Tokyo, Japan is responsible for the development of an outermost layer of the Vertex Detector (VXD). VXD is an innermost detector of Belle II, which play a role in precisely measuring position of decaying particles. In this thesis, the design of VXD, the ladder assembly procedure of the outermost later, mechanical alignment and quality control are presented.

Chapter 2

Belle II experiment

2.1 Physics motivation for upgrade

By November 2009, Belle experiment had been operated to collect 1040 fb^{-1} data sample. Although it contributed to the progress of high energy physics in many ways, the establishment of the mechanism of $\mathcal{CP}$ violation in quark sector was the most prominent one, where imaginary component(s) of Cabbibo-Kobayashi-Maskawa matrix (CKM matrix), a product of two matrices which diagonalize up or down types of quarks from weak interaction eigenstate to mass eigenstate, was the origin of this violation.

The CKM matrix can be expressed as

$$V = \begin{pmatrix} V_{ud} & V_{us} & V_{ub} \\ V_{cd} & V_{cs} & V_{cb} \\ V_{td} & V_{ts} & V_{tb} \end{pmatrix}$$

Because V must be unitary[1], its components are bound by following formula.

$$V^{\dagger}V = 1 \tag{2.1}$$

Consider to draw each term in the entries in formulae in Gauss plane. Figure 2.1 shows the situation. The vector formed by three terms make a triangle unless all terms are real. Therefore, existence of nonzero value of internal angle result in $\mathcal{CP}$ violation in weak quark sector.

Experimentally, we use following relation between distribution $A(\Delta t)$ and

[1] If it were not unitary, Lagrangian would not be real and this turns out to violate Lorenz invariance.

an angle ϕ_1 shown in Fig. 2.1.

$$\begin{cases} A(\Delta t) = \dfrac{\Gamma(B^0(\Delta t) \to f_{CP}) - \Gamma(\overline{B^0}(\Delta t) \to f_{CP})}{\Gamma(B^0(\Delta t) \to f_{CP}) + \Gamma(\overline{B^0}(\Delta t) \to f_{CP})} = S \sin(\Delta m \Delta t) \\ f_{CP} = J/\psi K_S \\ S = -\sin 2\phi_1 \end{cases} \tag{2.2}$$

where $\Gamma(\Delta t)$ is a decay rate such that difference of decay time between B^0 and $\overline{B}^0$ mesons is just Δt, and Δm is a mass difference of these mesons. The constant S is called asymmetry factor and represents the degree of $\mathcal{CP}$ violation. The definition depends on the final $\mathcal{CP}$-eigen state f_{CP}. Thus, by counting each spectrum with measuring the difference of the lifetime, we can measure the value of ϕ_1.

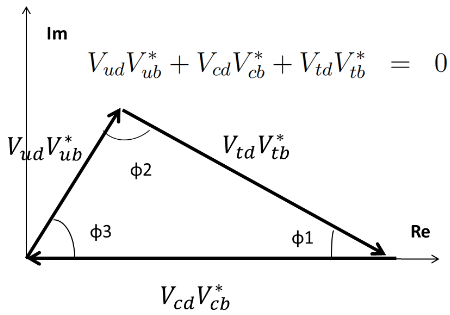

Figure 2.1: Drawings of each term in the (3,1)-entry of Eq. (2.1) in Gauss plane. Of all entries, this is experimentally important because the internal angles of the triangle turn out to be large. Recent global fit estimates their actual values as follows: $\phi_1 = (21.85 + 0.8 - 0.77)^\circ$, $\phi_2 = (91.1 \pm 4.3)^\circ$ and $\phi_3 = (67.1 \pm 4.3)^\circ$ [1].

Although the verification of the mechanism of the $\mathcal{CP}$ violation was a remarkable achievement, sign of new physics are still not yet statistically significant. Faced with that situation, Belle II experiment is planned to start to collect 50 times larger data than Belle sample from 2016 with SuperKEKB accelerator and Belle II detector, where not only luminosity of the accelerator is increased by a factor 40 but also improvement of the detector will be performed.

Among a lot of physics modes which are expected to observe signs of new physics, radiative $b \to s\gamma$ transition is known for its strong sensitivity to the new physics. As Fig. 2.2 shows, because of the absence of flavor changing neutral current in the standard model, tree level contribution is forbidden: only high order perturbation contributions (loops) are present. Therefore, the branching ratio is only $\sim 10^{-5}$. Moreover, parity asymmetry of weak force restricts its transition in either $b_R \to s_L\gamma_L$ or $b_L \to s_R\gamma_R$, where the subscript denotes left and right helicity of a particle. Therefore, not only are background of SM suppressed but also that is sensitive to L-R symmetric new physics models.

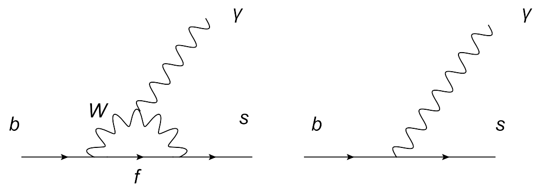

Figure 2.2: Feynman diagram of $b \to s\gamma$ transition. In the framework of the standard model, dominant contribution to $b \to s\gamma$ is via 1 loop (Left). Since there is no flavor changing neutral current, tree level diagram drawn in right side is forbidden.

If there should be L-R symmetric interactions, this contribution could be experimentally measured by time dependent analysis of B meson, where an increase of $\mathcal{CP}$-asymmetry factor S could be expected. In the standard model, this value is estimated to be $S \sim 0.04$ while L-R symmetric new physics models would lead this value to be 0.5. Figure 2.3 shows expected sensitivity of $b \to s\gamma$ transition. With the integrated luminosity 50 ab^{-1} of Belle II, the sensitivity reaches NP predictions.

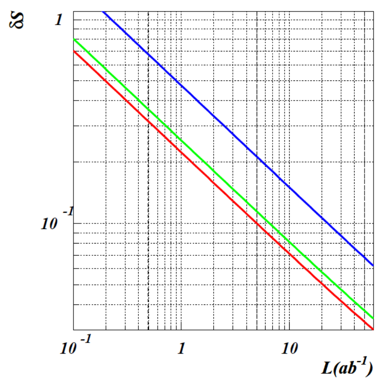

Figure 2.3: Expected sensitivity of time dependent analysis with respect to integrated luminosity. Red, green and blue line represent that of total $B \to K_S\pi^0\gamma$, $B \to K^{*0}\gamma \to K_S\pi^0\gamma$ and other $B \to K_S\pi^0\gamma$ respectively [2].

2.2 SuperKEKB accelerator

Figure 2.4 shows an overall view of SuperKEKB accelerator. In order to achieve the highest luminosity, *Nano-beam* scheme will be adopted in which vertical β function (this means size of beam), will be squeezed at interaction point (IP) by suppressing *hourglass effect* with relatively large crossing angle of 83 mrad [3]. Taking the increase of background into account, degree of beam asymmetry will be loosened from (E_{e^+},E_{e^-}) = (3.5 GeV, 8 GeV) to (4 GeV, 7 GeV), according to which boost factor $\beta\gamma$ will change from 0.43 to 0.28.

With the increase of luminosity of the accelerator, background sources not only proportional to luminosity such as Bhabha scattering and two photon process, but also unproportional factors such as Touschek effect, beam-gas scattering and synchrotron radiation, will increase. Therefore, Belle II detector must upgrade its tolerance for the high luminosity. The specification of SuperKEKB accelerator is summarized in Table 2.1.

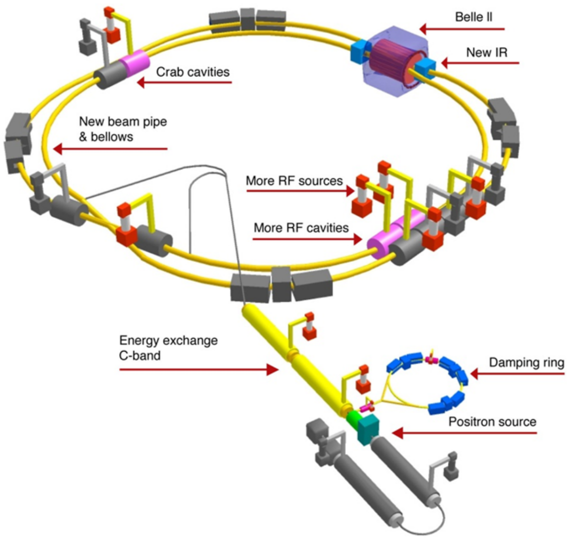

Figure 2.4: An overall view of SuperKEKB accelerator [4].This accelerator is composed of two types of rings, high energy ring (HER) for e^- and low energy ring (LER) for e^+ respectively, both of which are approximately 3km in perimeter. Electron and positron are accelerated directly by liner accelerator (sometimes this is called LINAC) up to 7 GeV and 4 GeV respectively and injected to individual rings.

Table 2.1: Parameters about SuperKEKB accelerator.

Parameters	Value
Energy (GeV)(e^+/e^-)	4.0/7.0
$\beta\gamma$	0.28
Current (A)	3.60/2.62
β_y^* (mm)	0.27/0.41
Luminosity(10^{34}cm^{-2}s^{-1})	80
Integrated luminosity (ab^{-1})	50
Crossing angle (mrad)	83
Perimeter of ring (km)	3

2.3 Belle II detector

Figure 2.5 shows a whole structure of the Belle II detector, which is composed of 7 subdetectors: PiXel Detector (PXD), Si-Strip Vertex Detector (SVD), Central Drift Chamber (CDC), Time Of Propagation counter (TOP), Aerogel Ring Imaging CHerenkov counter (ARICH), Electromagnetic CaLorimeter (ECL) and K_L and Muon detector (KLM), from inner to outer detector. Along with beam pipe, we summarize the information of these subdetectors in Table 2.2. For detailed information see Appendix A

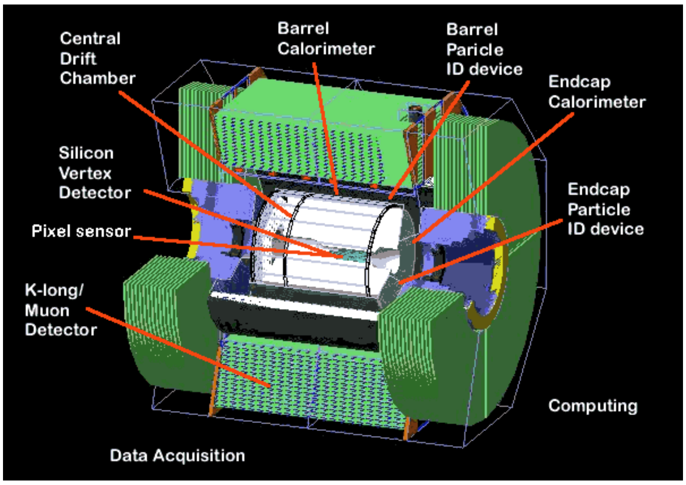

(a)

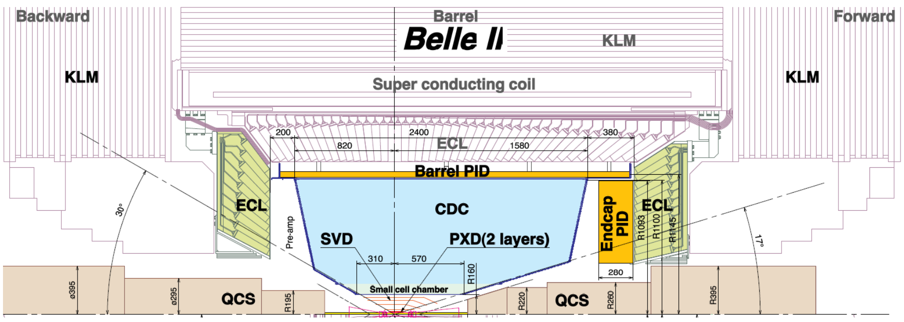

(b)

Figure 2.5: Whole structure of Belle II detector: drawing (a), cutoff (b) [5][6]. The Belle II detector has a barrel structure which encloses around IP. Magnetic field 1.5 T is supplied with a super conducting coil.

Table 2.2: Summary of subdetectors. The values are based on Belle II technical report [6].

Subdetector	Purpose	Configuration	Acceptance	Type	Specifications
Beampipe		$r_{\text{inner}} = 10$ (mm) $r_{\text{outer}} = 12$ (mm)		Beryllium	
PXD	Measure vertex position	$14 < r < 22$ (mm)	$17° < \theta < 150°$	DEPFET	impact parameter resolution $\sigma_z \sim 20\mu$m (PXD+SVD)
SVD	Measure vertex position	$38 < r < 135$ (mm)	$17° < \theta < 150°$	DSSD	K_S reconstruction efficiency 75%
CDC	Measure momentum dE/dx	$160 < r < 1130$ (mm) $-830 < z < 1590$(mm)	$17° < \theta < 150°$	Small cell drift chamber	$\sigma_{p_t}/p_t = \sqrt{(0.2\% p_t)^2 + (0.3\%/\beta)^2}$ $\sigma_{\mathrm{d}E/\mathrm{d}x} = 5\%$
TOP	Particle identification	$r \sim 1200$ (mm)		Quartz MCP-PMT	K/π separation: 99% at 0.5% pion misidentification
ARICH	Particle identification	$z = 1680$(mm)		Aerogel HAPD	K/π separation at 4 GeV/c: 96% at 1% pion misidentification
ECL	Measure energy	barrel: $1250 < r < 1620$ (mm) endcap: $z = -1020$ $z = 1960$ (mm)	$12.4° < \theta < 155.1°$	barrel: CsI(Tl) endcap: CsI	$\frac{\sigma_E}{E} = \frac{0.2\%}{E} \oplus \frac{1.6\%}{\sqrt[4]{E}} \oplus 1.2\%$ $\sigma_{pos} = 5$ mm$/\sqrt{E}$ (E in GeV)
KLM	Detect K_L & muon	barrel endcap	$20° < \theta < 155°$	barrel: RPC endcap: strip scintillator + RPC	$\sigma_{p_t}/p_t = 18\%$ for 1 GeV/c K_L

2.3.1 Definition of coordinate system of Belle II detector

For subsequent explanations, we define coordinate system of Belle II detector. Figure 2.6 shows the definition of direction of three axises x, y and z. With respect to z axis, ϕ is the azimuthal angle while θ is the zenith angle. Using these parameters, we also define $r = \sqrt{x^2 + y^2}$. Furthermore, within only this paper, we promise to use plane lower-case letters for components of Belle II coordinate system. Therefore, other notations such as x^* or X are not relevant to that of Belle II.

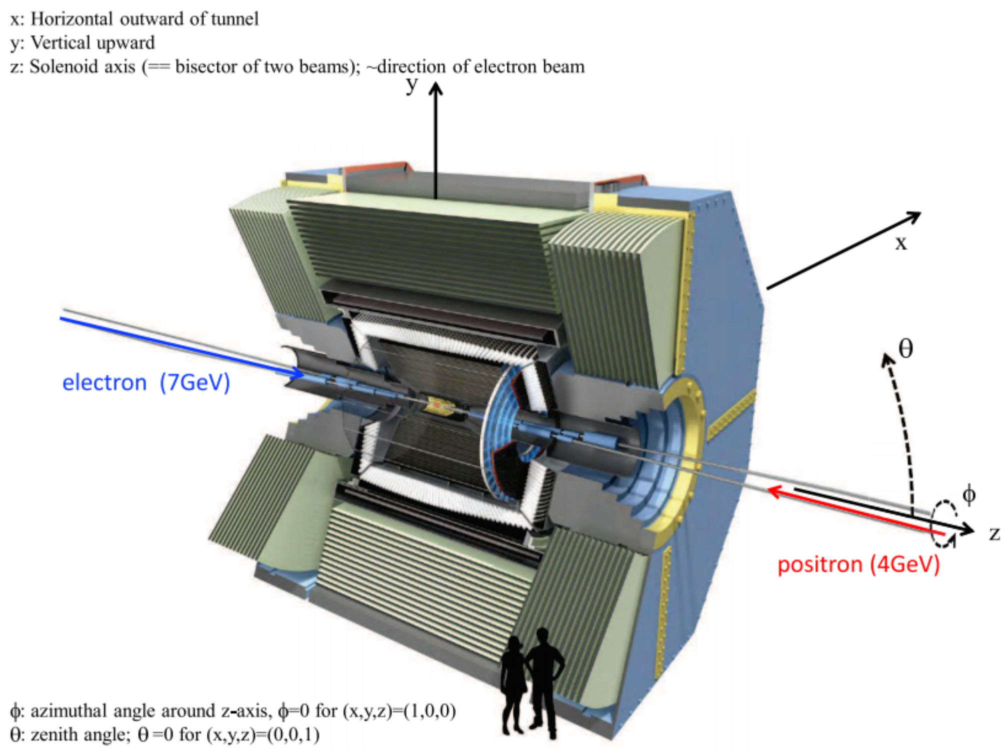

Figure 2.6: Definition of coordinate of Belle II detector. x, y and z represent horizontal outward of tunnel, vertical upward and solenoid axis respectively [8].

Chapter 3

Belle II vertex detector

As a vertex detector, two kinds of detectors, *Pixel detector* (PXD) and *Si-Strip Vertex detector* (SVD), will be installed into Belle II. Combining two different vertex detectors, we will be able to utilize both benefits and to achieve good performance as one vertex detector.

3.1 Vertex detector

A principal purpose of a vertex detector is to measure a position of vertex by measuring a hit position of charged particles. As we explained in Section 2.1, in the case of Belle II, distribution of difference of decay time between B^0 and $\overline{B}^0$ is used for search for new physics.

Figure 3.1 shows a typical example of $B^0\overline{B}^0$ decays. Since the average lifetime of B^0 mesons are very short (1.5 ps), it is impossible to directly measure the decay time. Therefore, by measuring the difference of flight length l, we calculate the difference of proper time t by $t = l/(\beta\gamma c)$. In order to measure l, tracks which are obtained from hit position are used. Although actual tracks become curved lines due to magnetic field, the principle does not change.

3.2 Requirement for Belle II vertex detectors

With the upgrade of the accelerator, we must also improve the detector. In this section, we show requirements for the vertex detector of the Belle II experiment.

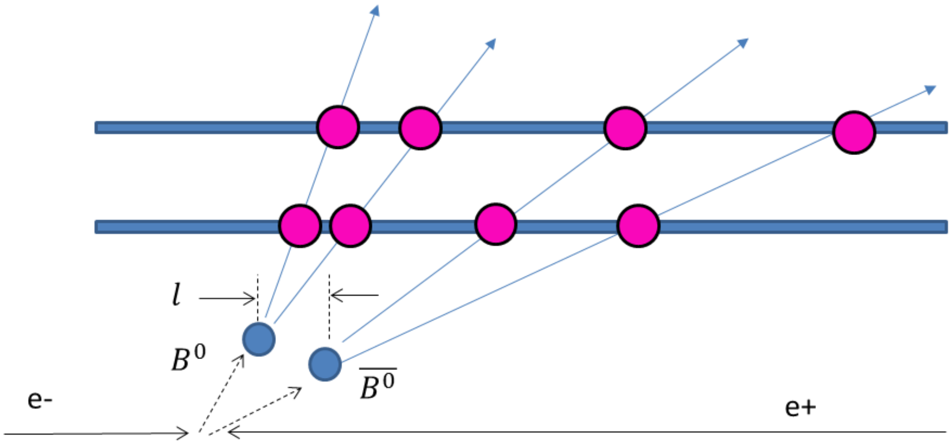

Figure 3.1: A role of vertex detector for Belle II. Difference of distance between $B^0\overline{B}^0$ vertices is measured. Red points represent hit position in layers of the vertex detector. Intersect points of obtained lines are regarded as decay point of particles.

3.2.1 Tolerance for high luminosity

The design luminosity of SuperKEKB is 8×10^{35} cm^{-2}s^{-1}, 40 times larger than the current world record achieved by KEKB. With a higher luminosity, the possibility of discovering new physics increases, but the background level at the detector also becomes higher. Particularly background source proportional to luminosity like QED process is a major problem for the vertex detector. Of all QED process, two-photon background shown in Fig. 3.2 is dominant, where beam electron-positron pair generates an extra pair.

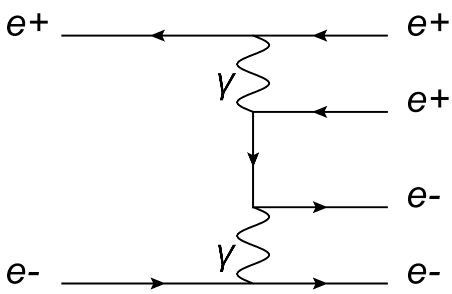

Figure 3.2: Two-photon QED process , major contribution to the background for the vertex detector of Belle II.

To evaluate the tolerance for high rate, occupancy is often used. This value is defined as a fraction of channels with hit in each triggered event. If the occupancy surpasses a certain degree of value, we can not correctly specify hit channel. For example, Fig. 3.3 shows a simulated value of SVD occupancy for Belle II in the assumption to use the same front-end chip as Belle SVD. If we assume to place the first the layer at 20 mm away from IP (since outer radius of beam pipe is 12 mm, this value would be practical), the occupancy becomes more than 100%. Because experience of Belle experiment suggests that the occupancy of SVD should be lower than approximately 10%, we must reduce the occupancy at least by a factor of ten.

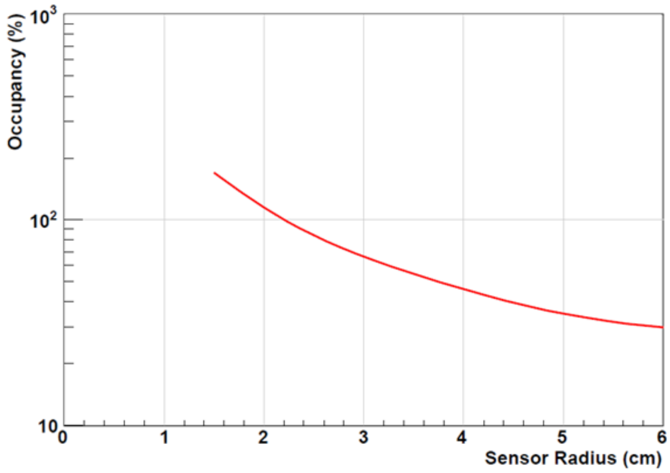

Figure 3.3: SVD occupancy at Belle II's case given that the same hardware as Belle is used [6]. Horizontal axis represents distance of layer from IP.

The problem with increasing luminosity is not restricted to occupancy. We must also cope with severe irradiation. Although estimation of dose is complicated, we can refer to an experience of Belle experiment again. According to radiation monitors positioned nearby Belle SVD, approximately 90 krad per ab^{-1} of integrated luminosity is estimated at the position 40 mm away from IP. Adding safety margin to a simple proportional calculation, total dose of 10 Mrad should be considered.

3.2.2 High spacial resolution

Vertex resolution

Because $\beta\gamma$ of Belle II is 0.28, average distance of B^0 flight would be roughly $c \times 1.5$ ps $\times 0.28 \sim 130$ μm. So if we would like to measure that lifetime, we need a vertex detector whose vertex resolution is sufficiently less than O(100 μm).

Impact parameter resolution

An impact parameter (distance between the point of closest approach of a track and primary vertex) resolution is commonly used for an evaluation of performance of vertex detectors.

Generally, impact parameter resolution can be expressed by

$$\sigma_i = \sqrt{a^2 + \left(\frac{b}{\overline{p_i}}\right)^2}, \quad i \ = \ z, \ r\phi \tag{3.1}$$

Here the first term represents a resolution determined by geometric factors such as a geometry of detector[1], an intrinsic resolution of each sensor and misalignment. The second term represents an effect of multiple scattering, where $\overline{p}_i$ is defined as

$$\overline{p_i} = \begin{cases} p \cdot \sin^{3/2}\theta, & i \ = \ z \\ \text{or} & \\ p \cdot \sin^{5/2}\theta, & i \ = r\phi \end{cases}$$

respectively, which compensates for an effective increase of length inside material caused by an angle θ, sometimes called *pseudo-momentum*. In order to decrease the value of a and b,

- short distance between innermost layer and IP,
- large distance between outermost layer and IP,
- good intrinsic resolution in each sensors,
- as little material between IP and the first measurement as possible,
- accurate alignment precision

should be appropriately maintained.

[1]For example, distance from IP, number of layers and relative position of individual layers.

Alignment precision

Of all these factors, precision of an alignment is largely relevant to systematic error of the time dependent analysis. For instance, in the measurement of the $\mathcal{CP}$ violation factor $\mathcal{S} \equiv \sin 2\phi_1$ using sample of $b \to c\bar{c}s$ transitions taken in Belle experiment, the result was $\mathcal{S} = 0.667 \pm 0.023$ (stat) ± 0.012 (syst), where the contribution of the misalignment of Belle SVD into the systematic error was $\delta\mathcal{S}_{\text{misalignment}} = 0.0024$ out of $\delta\mathcal{S}_{\text{total}} = 0.012$ [7]. Here the position of sensors were calculated using cosmic ray tracks and the misalignment compensated by software were 2 μm and 0.3 μm in horizontal and vertical directions respectively. In order not to disturb an improvement of precision thanks to large statistics of Belle II experiment, the position of sensors should not be out of alignment and be precisely measured in the production so that the software alignment can be performed with high reliability. This is one of main topics of this thesis and explained in Chapter 6.

3.2.3 Reconstruction efficiency of K_S

When we reconstruct B vertex in decay $B \to K^{*0}\gamma$, only two charged pions are observable as daughter particles of K_S decay. In order to determine decay vertex of K_S, at least two hit at vertex layers are required. Therefore, two outermost layers should be placed such that K_S decays are enclosed. Considering the fact that mean flight length of K_S is ~ 8 cm in this decay, distance of outer layer from IP is critical to the reconstruction efficiency of K_S.

3.3 Vertex detector for Belle II

Based on the requirement explained in Section 3.2, we fixed the design of the vertex detector. In this section, we introduce overall design and characteristics of Belle II vertex detector.

3.3.1 Layout of detectors

Figure 3.4 shows cut-off drawing of the vertex detector. The vertex detector is composed of stave parts called *ladders*. These layers of ladders enclose IP like a barrel.

Figure 3.5 shows cross section of the ladders. For inner two layers, we use pixel detectors. For outer four layers, we adopt Si-Strip Vertex detectors. It covers full Belle II angular acceptance from 17° to 150°. Number of ladders and distance of individual layers from IP are summarized in Table 3.1.

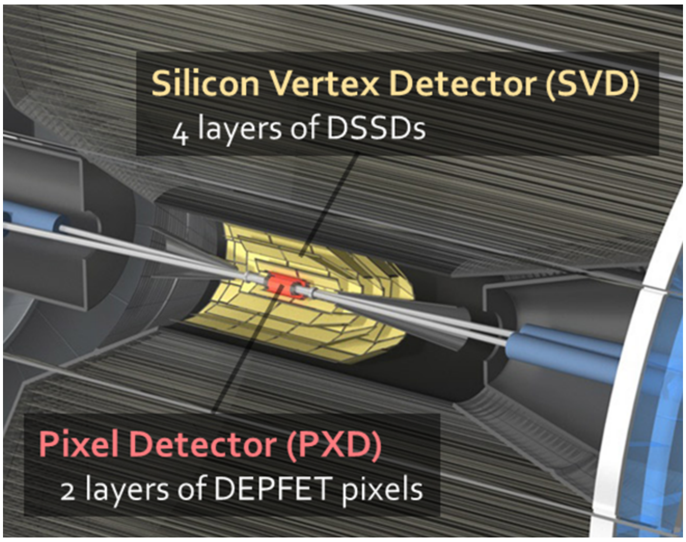

Figure 3.4: Cut-off drawing strcuture of Belle II vertex detector. Red and yellow objects represent the layers of PXD and SVD respectively. The layers are composed of multiple numbers of ladders.

Though as described in Subsection 3.2.2 the innermost (outermost) layer should be as close to (far from) IP as possible, actual position is constrained by a design of external structures: for inner side there is beam pipe whose outer radius is only 12 mm and for outer side there is CDC whose radius is 160 mm. These structure determine the overall dimension of the vertex detector.

The position of layer 5 was determined by considering a reconstruction efficiency of K_S. Figure 3.6 shows a fraction of K_S vertex within distance from IP for decay $B \to K^{*0}\gamma$. By positioning layer 5 relatively close to layer 6, high K_S reconstruction efficiency of 75% is achieved.

Table 3.1: Number of ladders. L1 and L2 are PXDs, and L3-L6 are SVDs.

Layer	L1	L2	L3	L4	L5	L6
Distance from IP (mm)	14	22	38	80	104	135
Number of ladders	8	12	7	10	12	16

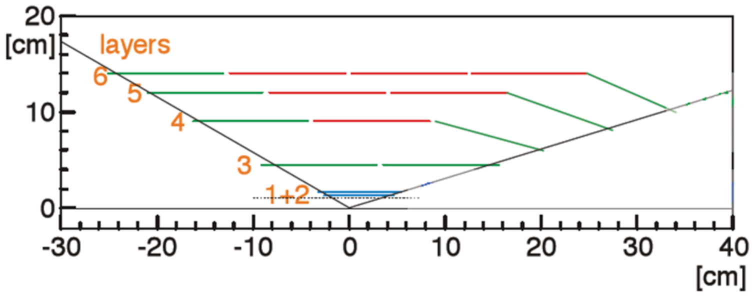

Figure 3.5: A cross section of vertex detector in yz plane. The acceptance of is from 17° to 150° [6]. Colors of SVD represent kinds of module: green is a forward or backward module, red is a Origami module. This will be explained in Chapter 4.

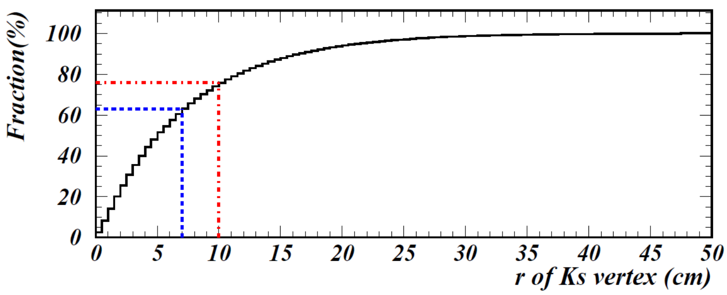

Figure 3.6: Fraction of K_S vertex within distance from IP for $B \to K^{*0}\gamma$. The blue dashed line is the location of second outermost layer of Belle SVD and red corresponds to that of Belle II SVD [9].

3.3.2 Slant structure

The characteristic part of the design would be a *slant* structure for forward parts. As shown in Fig. 3.7, the trajectory of particle inside sensor becomes shorter than that of normal one. If the slant angle is θ_s, the path length inside sensor is proportional to an inverse of $\sin(\theta + \theta_s)$. Since θ of the edge of forward side is 17° and thickness of our DSSD is 300 μm, flight of particle inside forward sensor of layer 6 (θ_s of layer 6 is 21.1°) becomes $300\ \mu\text{m}/\sin(17^\circ + 21.1^\circ) \sim 490\ \mu\text{m}$. If it were not for the slant angle, this number would be 1030 μm. The decrease of length results in suppression of multiple scattering by a factor of 1.7 for scattering angle. Although this structure makes the ladder assembly difficult, this contributes improvement of impact parameter resolution.

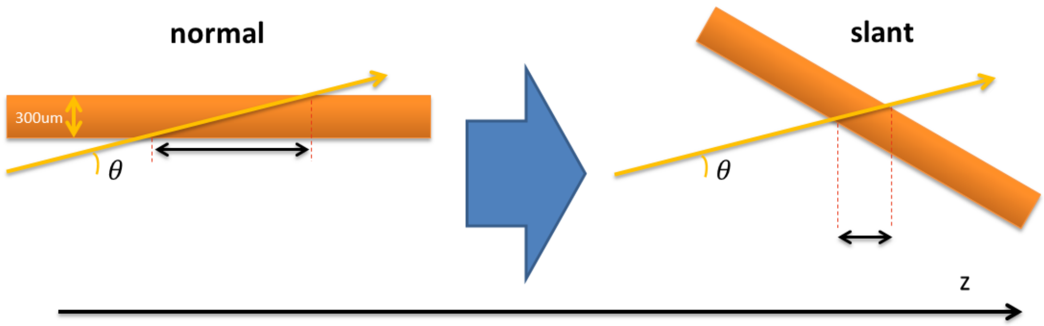

Figure 3.7: The slant structure contributes higher precision by decreasing the distance of charged particle traveling inside DSSD.

3.3.3 Pixel detector (PXD)

The effective area of pixel detector is, as the name suggests, cell structure. Because every pixel is isolated from each other, we can specify the hit position in two dimensional space. The Belle II PXD adopts Depleted Field Effect transistor (DEPFET) as its sensor, which can be light including peripheral materials.

Structure of PXD

Figure 3.8 shows a whole structure of the pixel detector. This detector is composed of two layers which correspond to 17 M pixels in total. As an acceptance, full range from 17° to 150° is covered. The readout electronics

Table 3.2: Pixel ladders parameters

	# ladders	r from IP (mm)	# pixels ($z \times r\phi$)	pixel size[2] ($z \times r\phi$) (μm^2)	sensitive area ($z \times r\phi$) (mm^2)
Layer 1	8	14	768×250	55×50 / 60×50	44.80×12.5
Layer 2	12	22	768×250	70×50 / 85×50	61.44×12.5

are placed on both ends of each ladder (outside the acceptance). We show parameters of pixel detector in Table 3.2.

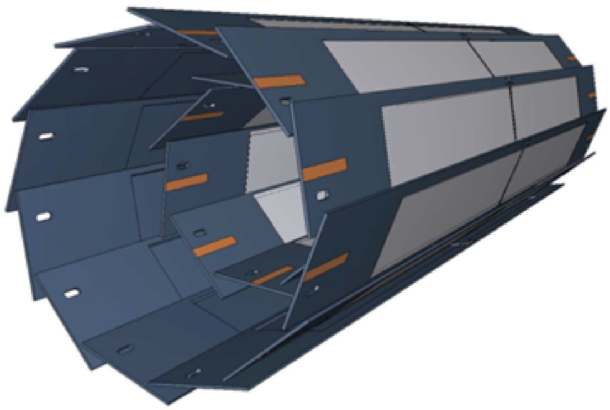

Figure 3.8: Whole structure of the PXD. The light gray surfaces are sensitive area of DEPFET [6].

DEPFET sensors

A DEPleted Field Effect Transitor (DEPFET) is a sensor which combines the features of pixel devices and depleted semiconductor. We present the internal structure of DEPFET transistor in Fig. 3.9. A p-channel-junction-field-effect transistor is formed onto silicon, which plays a role in amplifying excited charges that are collected by minimum potential in the depletion region. When incident charged particles enter the sensor, excited electrons are accumulated in the potential minimum, called *internal gate*. If we turn on the gate of the transistor in the normal way, current proportional to the accumulated charges flows.[3] To remove the collected internal charges, a clear

[2]There are two regions and pixel sizes depend on them.
[3]The gain is 0.5 nA/e.

gate is turned on.

Thanks to its internal amplification, the DEPFET can be thinned down to 75 μm without losing sensitivity, decreasing an effect of multiple scattering. This thickness corresponds to $0.19\% X_0$.

In addition to above features, DEPFET has a remarkable property in terms of its power consumption. Since there is no current flow in DEPFET cells except read out period, total power consumption is 180 W in total. This value is relatively low in spite of its large number of cells. Hence heat removal of DEPFET can be done from the support structure of PXD located at both ends of the ladder.

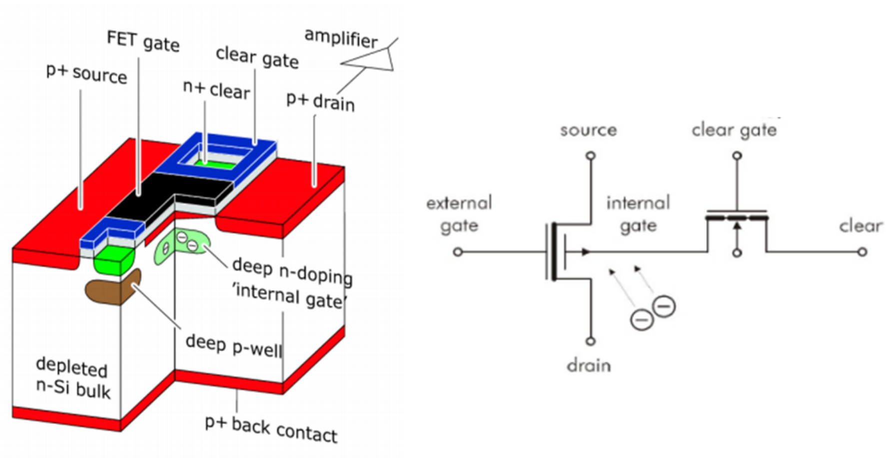

Figure 3.9: Internal structure and circuit of DEPFET sensor [6].

High tolerance for Occupancy

Towards the severe background environment of Belle II detector, PXD has a satisfactory tolerance for the occupancy since the sensitive regions are isolated one another. According to Monte Carlo simulations, the occupancy of the first layer was estimated to be less than 0.5%.

Spatial resolution

If we assume to use only one pixel to locate the hit position of particle, the intrinsic resolution becomes $\sigma_z = d/\sqrt{12}$ within the range in which contribution of multiple scattering are ignored.[4] Here d is a size of pixel. Since

[4]For the reason of the factor $\sqrt{12}$, see Appendix C.1.

d is approximately 50 μm, the intrinsic resolution of PXD turns out to be $\sim 15\mu$m.

Readout

Assuming trigger rate of 30 kHz, occupancy 2%, data width 4 bytes and total amount of pixels 11 M, amount of total data rate from PXD becomes $11\text{M} \times 0.02 \times 30\text{K} \times 4\text{byte} \sim 30\text{GB/s}$. Since it is not possible to save all data, we have to reduce information into only meaningful ones on online computing. For that purpose, PXD utilizes tracking information from SVD and CDC to restrict region-of-interest (ROI) and reduces the data size down to one tenth of the original.

3.3.4 Silicon Vertex Detector (SVD)

Unlike the case of PXD, the Belle II SVD has linear effective areas (we call this line strips). These lines are orthogonally arranged and it allows us to get horizontal information of incoming charged particle. In this section, we show only an overview of SVD. More detail will be give in Chapter 4.

Structure of SVD

Figure 3.10 shows a drawing of the whole structure of SVD. The SVD is composed of four layers, from layer 3 to layer 6 , which corresponds to approximately 240 K of strips and 1.2 m^2 of the effective area in total. Specification of each layer is given in Table 3.3.

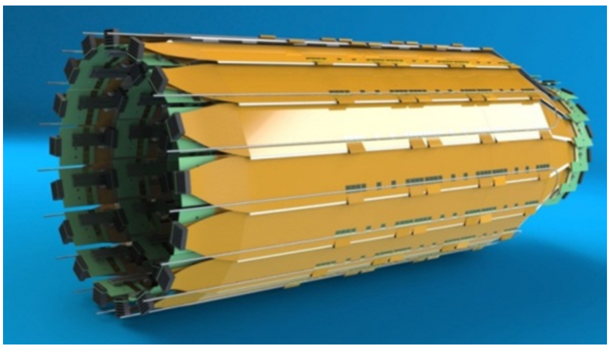

Figure 3.10: Drawing of the whole structure of SVD [10]. The khaki object represents Origami flexible boards. Green ones on both ends are hybrid boards which play a role in processing signals from forward and backward DSSD.

Table 3.3: Parameters of SVD layers

Layer	# ladders	r from IP (mm)	length (mm)	# strips[5] z	# strips[5] $r\phi$	slant angle (deg)	sensitive area (mm^2)
3	8	38	262	768×2	768×2	-	9474
4	10	80	390	512×3	768×3	11.9	18798
5	14	104	516	512×4	768×4	17.2	25827
6	16	135	645	512×5	768×5	21.1	32857

DSSD (Double-sided Si-Strip Detector)

As a sensor of SVD, we use Double-sided Si-Strip Detector (DSSD). Fig. 3.11 is a picture of DSSD. Because n and p-type strips are orthogonally allocated along z and $r\phi$ axis, we can horizontally locate positions of incoming particles. The right drawing shows a structure of DSSD. We apply reverse bias voltage of ∼80V between electrodes. This bias voltage makes the sensor fully depleted and resistance between n and p becomes insulated state. Here p$^+$ stops play a role in keeping the isolation between n$^+$ strips. When a charged particle enters inside depletion region, excited electron-hole pairs are drifted and absorbed into electrodes according to the electrical field.

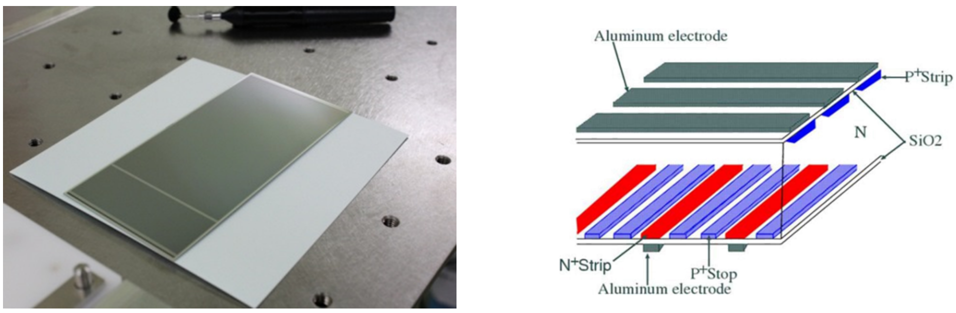

Figure 3.11: Picture of large rectangular DSSD used for layer 4 to layer 6 (left) and drawing of a structure of DSSD (right). Two different types of strips are orthogonally allocated which enables us to locate a position of an incoming particle.

Table 3.4 is a list of parameters of DSSDs. Three kinds of DSSDs are used: trapezoidal sensor for slant part of layer 4 to layer 6, large rectangle sensor for flat part of layer 4 to layer 6 and small rectangle sensor for layer

[5]For example, 512×3 means that there are three sensors which has 512 strips along z axis.

Table 3.4: Parameters about DSSDs. L means layer. Used numbers are per one ladder.

Sensor type	# strips (P)	# strips (N)	Pitches z (μm)	Pitches $r\phi$ (μm)	Thickness (μm)	# used for L3	# used for L4	# used for L5	# used for L6
S-rectangular	768	768	160	50	320	2	0	0	0
L-rectangular	768	512	240	75	320	0	2	3	4
Trapezoidal	768	512	240	50-75	300	0	1	1	1

3. Since layer-3 DSSDs are very close to IP, not only are pitches smaller, but also the number of strips is larger than other layers.

We attached detailed information such as the dimension, number of strips and electric specification in Appendix B.

Intrinsic resolution

In order to achieve satisfactory performance in vertex resolution, intrinsic resolution of each layer should be appropriately maintained. What are mainly important to determine the intrinsic resolution of SVD are pitch of strips and signal to noise ratio (SNR).

Fig. 3.12 shows expected intrinsic resolution of Belle II's SVD. Fineness of pitches of DSSDs along $r\phi$ direction is reflected in resolution. The better spatial resolution than pitches of DSSDs comes from the method to locate the incident particle. For more detail, see Appendix C.

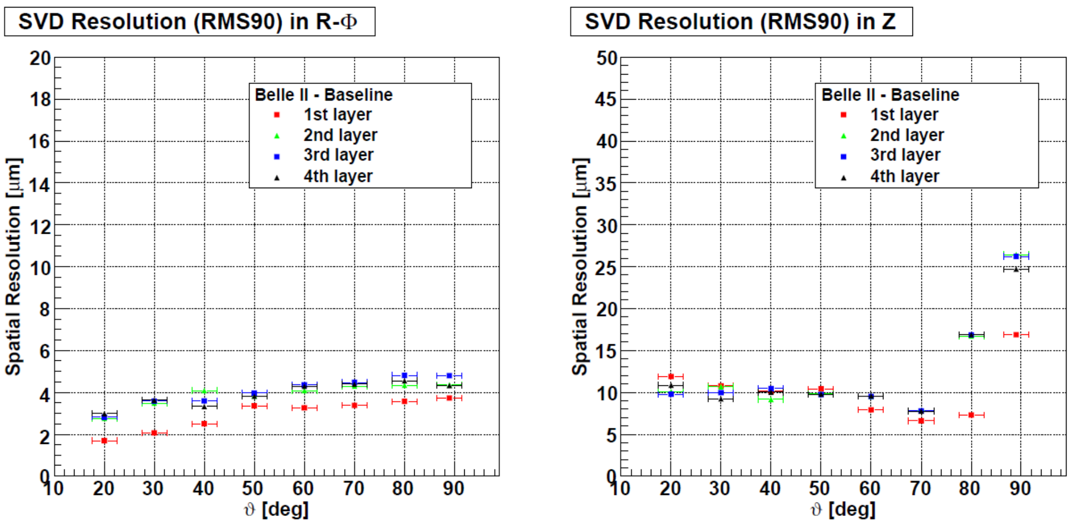

Figure 3.12: Expected intrinsic resolution of each layer in $r\phi$ and z direction. In these drawings first to fourth are suffices of SVD. For instance, 1st means layer 3 [6]. Horizontal axis is an incoming angle θ of particles.

Table 3.5: Expected performance of Belle II vertex detector compared to that of Belle SVD.

Quantity	Value of Belle II VXD	Value of Belle SVD
Material budget	$0.19\% X_0$ per one layer (L1-L2) $0.57\% X_0$ per one layer (L3-L6) $2.7\% X_0$ in total	 $0.47\% X_0$ (L1-L4) $1.9\% X_0$ in total
Impact parameter resolution (z) p =500 MeV p =1.0 GeV	 $\sim 25\ \mu$m PXD+SVD $\sim 18\ \mu$m PXD+SVD	 $\sim\ 80\ \mu$m $\sim\ 50\ \mu$m
Acceptance	$17° < \theta < 150°$ $0° < \phi < 360°$	$17° < \theta < 150°$ $0° < \phi < 360°$
Sensitive range	14 mm $< r <$ 135 mm	20 mm $< r <$ 88 mm
Estimated occupancy	0.5% (L1), $<$ 10%(L3)	
Reconstruction efficiency of K_S	75%	60%
Power consumption	180 W (total PXD) 660 W (total SVD)	

3.3.5 Performance of Belle II vertex detector

We show overall performance of the Belle II vertex detector in Table 3.5. Points of upgrade from Belle SVD are good performance of impact parameter resolution and improvement of reconstruction efficiency of K_S. Figure 3.13 shows the impact parameter resolution of Belle SVD and Belle II vertex detector. We can see an improvement of the impact parameter resolution over a broad range of momentum.

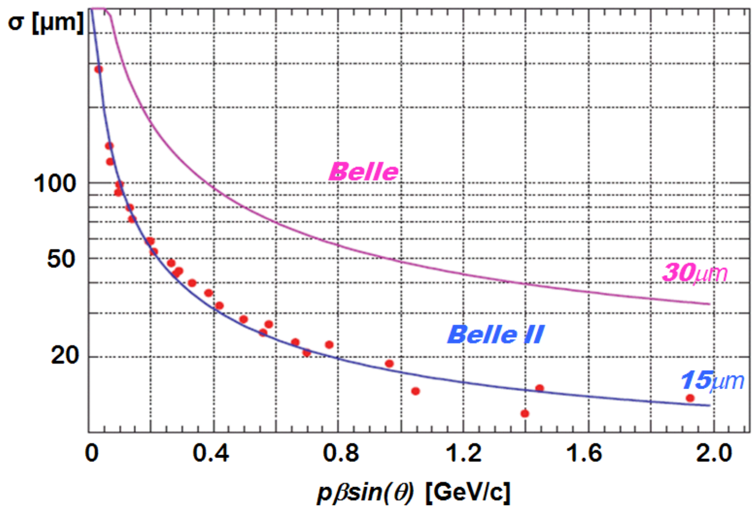

Figure 3.13: Impact parameter resolution of the Belle SVD and Belle II vertex detector along z axis.

Chapter 4

Components of SVD

As described in the last chapter, SVD (Si-Strip vertex detector) is a detector which uses DSSDs to measure the hit position of incident charged particles. The challenging requirement for Belle II SVD is its processing speed and tolerance for radiation owing to high luminosity of SuperKEKB. The occupancy of the innermost later must be less than 10%. The detector must have radiation tolerance for more than 10 Mrad of irradiation. In this chapter, we explain the comportments of SVD which enable us to achieve these requirements.

4.1 Front-end electronics of SVD

4.1.1 Front-end readout APV25

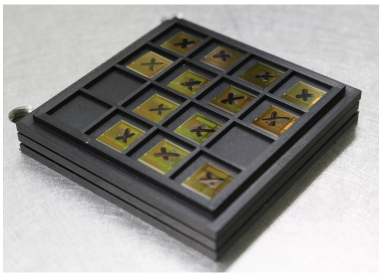

Figure 4.1: Front-end chips APV25.

APV25 front-end chips, originally developed for CMS tracker, were chosen for front-end readout chips for the Belle II SVD, because this chip meets all requirements. Not only fast shaping time but tolerance for radiation is the reason why we adopted this chip. Figure 4.1 and 4.2 show a photograph and block diagram of the APV25. The APV25 chip has 128 identical circuits composed of low-noise preamplifiers followed by time variable shaper (50-200 ns). All channels have 192-cell ring buffer and each signal is stored at a 40 MHz frequency. This chip can tolerate 30 Mrad of dose, which corresponds to threefold our goal.

Thanks to the fast shaping time (50 ns) of the APV25, time over threshold is only 160 ns. If we compare the situation to VA1TA (shaping time 800 ns and time above threshold 2000 ns), this chip can improve occupancy by a factor of 12.5. Moreover, in order to narrow down effective shaping time much more, the hit signals are fit to smooth function and used to confine hit time. This method makes effective shaping time 3 ns, which corresponds to 20 ns above threshold. Consequently, this improvement by a factor of 100 enables us to decrease the occupancy of layer 3 to be less than 10%. This is summarized in Fig. 4.3.

For more information about APV25, refer to user's manual of this chip [12].

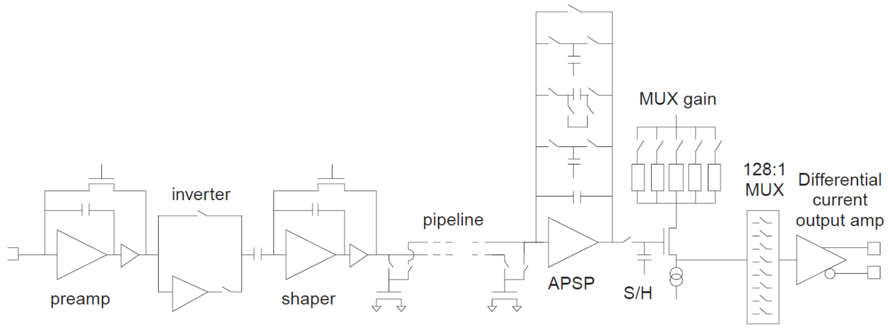

Figure 4.2: Building blocks of APV25 [10].

4.1.2 Origami chip-on-sensor concept

There are a lot of factors which determine the intrinsic resolution of SVD. Among all, signal to noise ratio (SNR) is one of the most important factors, because position of incoming particle is calculated by using strength of signals in the clusters of strips. [1] In order to achieve a good performance in SNR, we should put front-end chips as close to signal sources as possible, because the noise is proportional to capacitance of input. In many cases of vertex

[1]See Appendix C for details of this method.

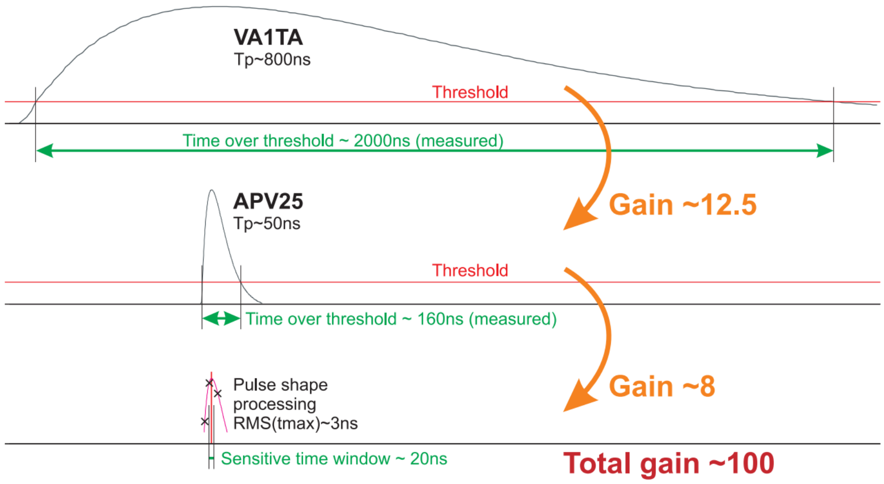

Figure 4.3: Improvement of occupancy from Belle SVD[6]. By adopting APV25 chips, time over threshold is improved by a factor of 12.5 and fitting procedure on FPGA processing enables us to further improve effective occupancy by a factor of 8.

detectors, however, so as to avoid extra material budget, front-end chips as well as any materials, tend to be put outside an acceptance. That results in higher capacitance.

Considering that SVD of Belle Ⅱ is relatively large, we gave up to put front-end chips outside acceptance and decided to adopt *Origami chip-on-sensor concept*, where we locate front-end chips on DSSDs. This layout makes it possible to amplify signals nearby sources. In order to connect DSSDs and the APV25 chips, readout fanout, *pitch adapter (PA)* is wrapped around the corner of DSSD as shown in Fig.4.4. The additional material is minimized by thinning the APV25 chips from original 300 μm to 100 μm.

To evaluate the improvement which comes from Origami concept, beam test was performed in 2008 and 2009 when two specialized evaluation boards were tested: one was the conventional module and another was a module applied Origami concept. According to the result, an increase of SNR by a factor of 1.3 was achieved [11]. In the beam test of *2-Origami module* in 2012, indeed which is a portion of the actual ladder, SNR was measured to be 12.6 for p side and 21.7 for n side.

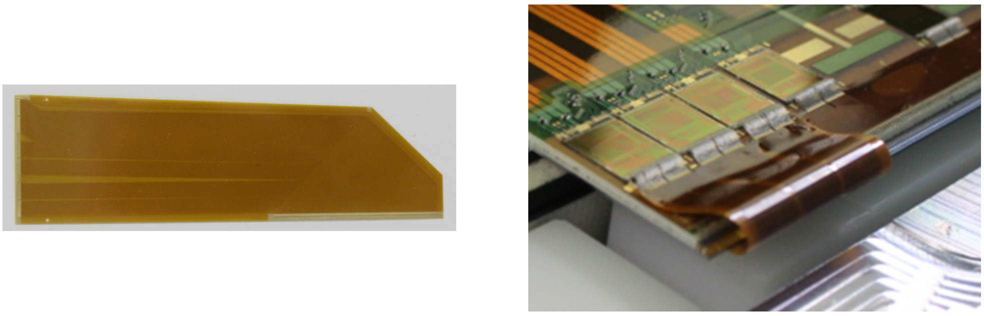

Figure 4.4: Left picture shows fanout called *pitch adapter* 2 (PA2). Right picture shows the situation of wrapping of PA2. By bending the fanout, the distance from signals is minimized.

4.2 Back-end of SVD

Fig. 4.5 shows a schematic view of the readout chain of Belle II SVD. The APV25 chips amplify signals from DSSDs and transmit the analog signal toward fast-analog-to-digital converter (FADC) unit via junction box (this supplies power for APV25).[2] Low output impedance of the APV25 enables us to transmit signals by as long as 12 m (distance between the APV25 and FADC+FPGA board).

Transmitted analog signals are converted to digital signals on FADC+FPGA board followed by online signal processing such as waveform shaping, pedestal reduction and hit time fitting.

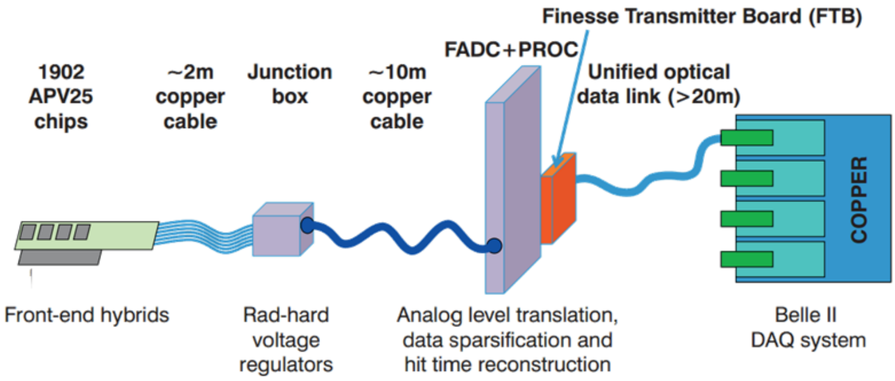

Figure 4.5: Drawing of readout chain of Belle II SVD [6].

[2]Furthermore, this junction box plays a role to avoid long cables being attached to the detector during installation.

4.3 Structure of layer-6 ladder

As mentioned in Chapter 1, main theme of this thesis is mechanical quality management of layer-6 ladder. Therefore, we confine the topic to layer 6.

The structure of SVD is comprised of ladders. By adopting the this structure, production of SVD resolves to the repetition of ladder assembly. Figure 4.6 shows a drawing of the ladder. On top of ladder, FLEX board, front-end chips, thermal isolation form are located. The bone-like parts called *rib* supports whole structure of ladder.

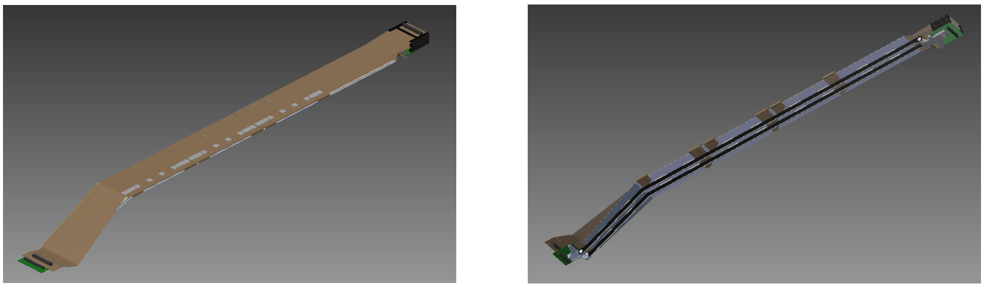

Figure 4.6: Top and bottom view of ladder. The lower side is forward.

4.3.1 Components of layer-6 ladders

Fig. 4.7 shows all components of the ladder. The main structure of layer-6 ladder is composed of two **Ribs**, five **DSSDs**, two **Airexes** (a board inserted for insulation), three variant **Origami** FLEXes (name of flexible board) and fifty **APV25s** in the order from bottom to top. In addition to them, there are six kinds of **Pitch Adapters** (PAs), two **Hybrid boards** and two **Mount blocks** for backward and forward.

The structure of the ladders can be resolved into three modules: forward module, Origami module and backward module. Here forward and backward modules are comprised of one DSSD and one hybrid board, while Origami module is made of three DSSDs, Airex and Origami flexible board. These modules are illustrated in Fig. 4.8.

Ribs

The main support structure of the ladder called *Rib* is shown in Fig 4.9. It is required to be light as well as stiff because of suppression of multiple scattering. To achieve both goals, we adopt the structure of a sandwich of CFRP

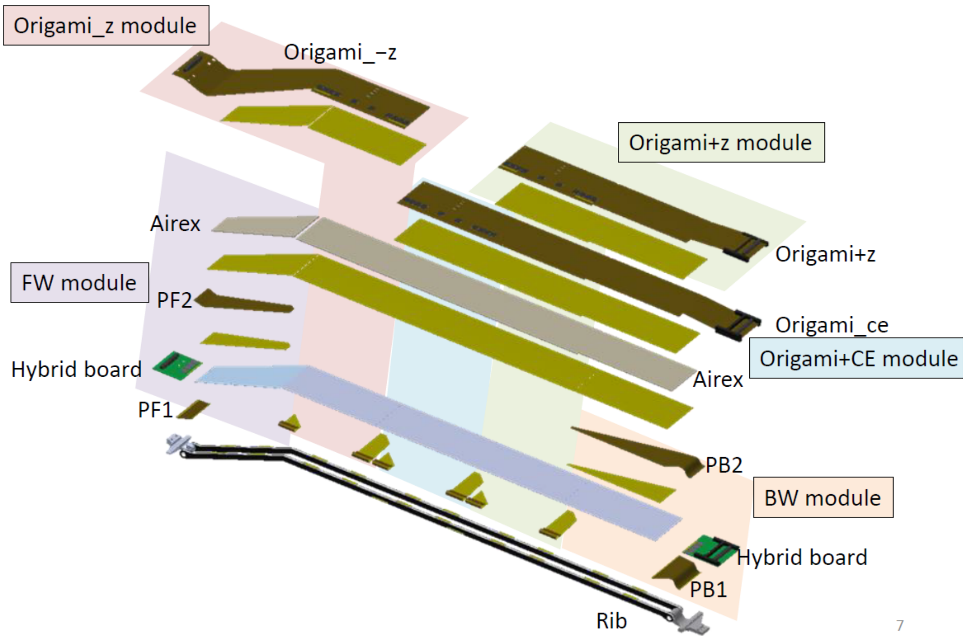

Figure 4.7: Components of the full ladders for layer 6. In this layer we use five DSSDs. Only forward DSSD has different shape (trapezoidal) from the others. The readout of forward and backward DSSDs are done on hybrid boards located at both ends. On the other hand, readout of three DSSDs in the middle are processed on three variants of flexible circuit boards, which are called *Origami*. Every signal is transfered outward via connectors at ends of forward and backward.

(carbon-fiber-reinforced plastic) and Airex (kind of polymer foam). By combining the stiffness of CFRP and the lightness of Airex, rib can support the ladder with a minimum material.

DSSDs

As explained before, we use DSSDs for the SVD ladders. In our case, DSSDs are placed such that n-side strip points upward and p-side downward. Since we have already introduced rectangle sensor (Fig.3.11), here we present a photograph of only trapezoidal sensor in Fig. 4.10

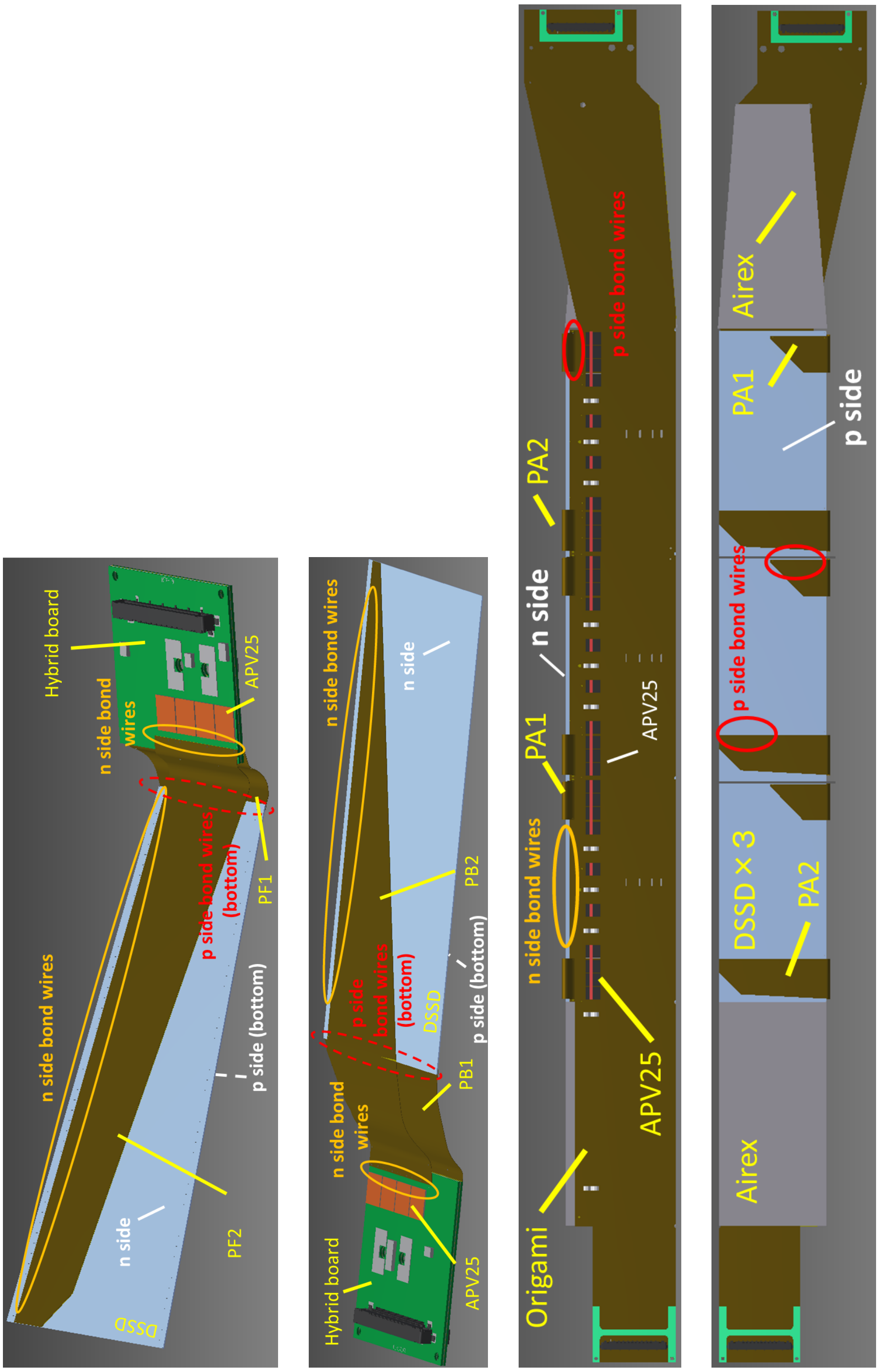

(a) Forward module (b) Backward module (c) Origami module on top view (d) Origami module on bottom view

Figure 4.8: Drawings of forward module, backward module and Origami module.

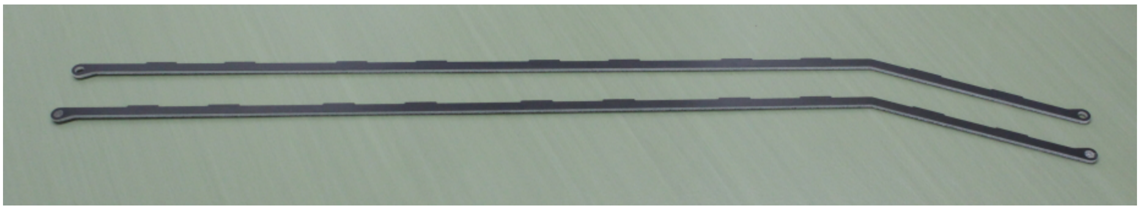

Figure 4.9: Picture of ribs for layer 6.

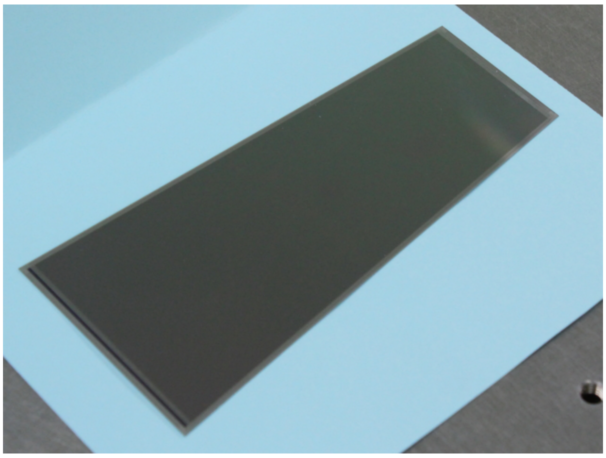

Figure 4.10: A trapezoidal DSSD used for slant part.

Airex

Between DSSDs and Origami, we insert *Airex* as an isolator of not only electricity but also heat. Although Airex is a name of a product, we do not use directly the original ones but compress them in order to make them stiffer.[3] The features of this material are high strength, stiffness to weight ratios and thermal insulation. We show a photograph of Airex in Fig. 4.11.

Origami

Origami is a name of main flexible circuit board of the ladder. As the name suggests, we adopt a structure of bending for fanouts. We show a photograph of Origami in Fig. 4.12.

In layer 6, we use three types of Origamis: Origami-z, OrigamiCE and Origami+z. The suffixes, -z, CE, +z, mean their positions along beam axis.

[3] In order to achieve good bondability, we need stiffness as a carpet of pads.

Figure 4.11: Picture of Airex offered by Airex AG CO. Sins, Switzerland.

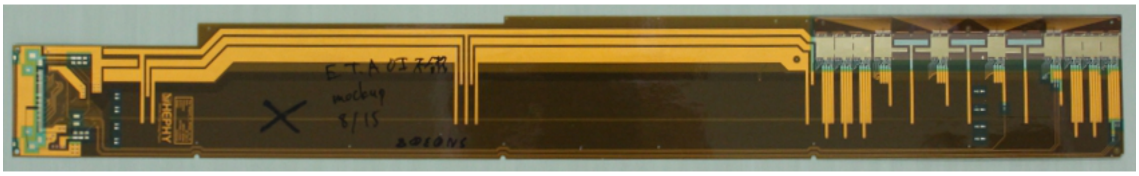

Figure 4.12: Picture of Origami.

Each Origami has ten APV25 chips and processes signals from one DSSD which corresponds to 768 p strips, and 512 n strips.

Pitch Adapters

Figure 4.13 shows photographs of the fanouts of Belle II SVD, called pitch adapter (PA). There are six types of pitch adapters: PF1/PF2 for a forward DSSD, PA1/PA2 for three DSSDs at center of ladder and PB1/PB2 for a backward DSSD. The role of pitch adapters is to connect different pitch electrodes of DSSDs to the APV25 chips. While the PF1 of PB1 are used for reading out p-side strips, PF2 and PB2 are used for n-side. In contrast, both PA1 and PA2 read out p-side signals since n-strips of three center DSSDs are directly connected to Origami. These are illustrated in Fig. 4.8. Information of pitch adapters are summarized in Table 4.1.

(a) PB2

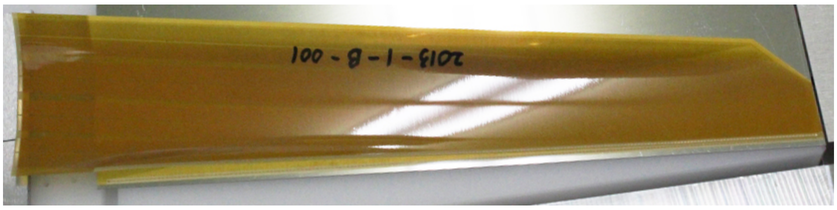

(b) PF2

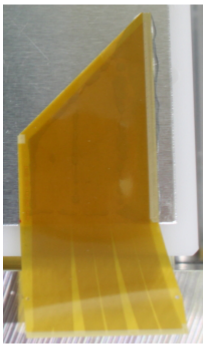

(c) PA1

(d) PA2

(e) PF1

(f) PB1

Figure 4.13: Fanouts of Belle II SVD, called pitch adapters. While B and F stand for backward and forward respectively, letter A does not mean its position.

Table 4.1: Parameters of pitch adapters.

Name	Connect	# Connections	# used for L6	Comment
PA1	p	384	3	Wrapped around the corner
PA2	p	384	3	Wrapped around the corner
PF1	p	768	1	
PF2	n	512	1	
PB1	p	768	1	
PB2	n	512	1	

Hybrid boards

Signals from backward and forward DSSDs are amplified on boards located at both ends of the ladder, called *Hybrid board*. Signals read out by PF1, PF2, PB1 and PB2 are transfered to the APV25 chips on these boards. Through the connector, amplified signals are transmitted to FADC/FPGA boards. We show a photograph of Hybrid board in Fig. 4.14.

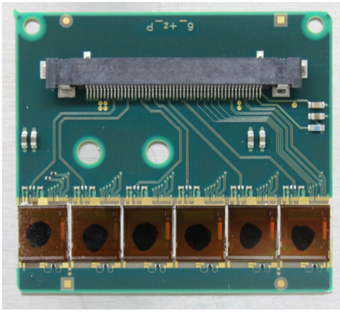

Figure 4.14: Picture of the Hybrid board. APV25 are mounted on this board. The amplified signals from APV25 are directly conveyed outside via connectors.

Mount blocks

Figure 4.15 is a photograph of *mount blocks*. These parts play a role in fixing the structure of ladders. By penetrating precise pins through the holes, we mount ladders on end rings.[4] In addition, the holes are used for a definition of a coordinate of the ladder.

Figure 4.15: The backward mount block

[4]End ring is a support structure of the ladders at both ends.

Chapter 5

Assembly of SVD ladder

In this chapter, we explain the ladder assembly procedures.

5.1 Full ladder assembly procedures

Figure 5.1 shows a flow of full ladder assembly procedures. As we mentioned in the last chapter, the ladder consists of forward, Origami and backward modules. The ladder assembly procedure is divided into six steps.

The first step is called *common procedure*. Three DSSDs glued with PAs are placed on *assembly-bench*; here the *assembly-bench* is a name of a jig and plays a central role in the assembly of the ladder. Consequently these three DSSDs become a portion of the Origami module. Other two DSSDs placed on both ends become forward and backward modules. After the preparation of five DSSDs, we precisely align DSSDs in a plane of the *assembly-bench*. This is the last process in which we control the alignment of DSSDs and this must be kept in the following procedures.

Of these five DSSDs, two DSSD at both ends are separately assembled into forward and backward modules respectively, where we glue pitch adapters and bond wires. These two modules are glued with rib. These procedures can be separately performed without interfering with Origami module assembly.

Three DSSDs are assembled into the Origami module. The aligned DSSDs are glued with the Airex and Origami before wire-bonding between n-side strips and Origami. Next we wrap PA1 and PA2 around the corner of DSSDs and glue them with Origami. After waiting for glue curing, we bond wires between PAs and the APV25 chips. Figure 4.8c and 4.8d are drawings of Origami module.

Finally Origami module and rib are combined to finish ladder. Here me-

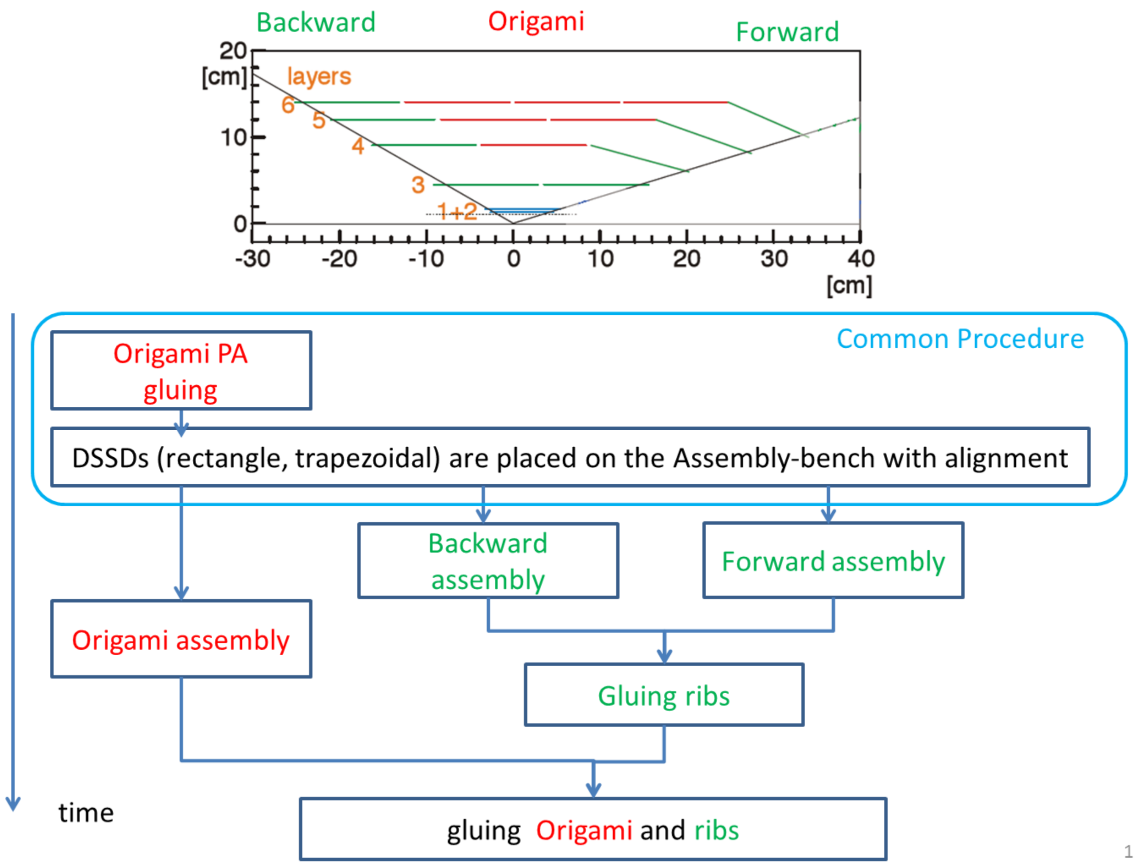

Figure 5.1: The flow of the full ladder assembly procedures. All assembly procedures are divided into six blocks: common procedures, Origami assembly, backward assembly, forward assembly, gluing with rib and final gluing procedures

chanical and electrical quality assurance are performed towards the finished ladder.

Including wire bonding and waiting time for curing glue, we estimate 25 working days to assemble the one ladder.

5.2 Ladder assembly jigs

Ladder assembly tasks are performed on support fixture called jigs. Jigs allow us to assemble the ladder uniformly, precisely, stably and independently of operator's skill.

Exchange of samples between two jigs are done by vacuum chucking. As is shown in Fig. 5.2, if we would like to transfer a DSSD from one end to another, we apply vacuum to only one side of jig.

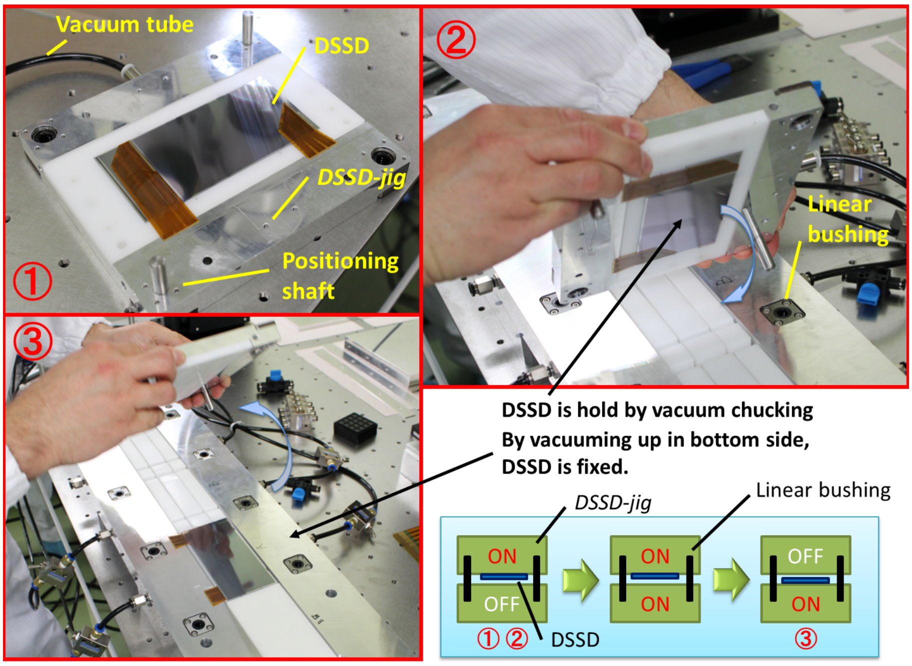

Figure 5.2: Exchange of a DSSD between jigs. The DSSD is hold and exchanged by vacuum chucking. The relative position of jig is fixed by linear bushings.

In order to fix relative position of jigs, linear bushings are used. Figure 5.3 and 5.4 show a photograph and an internal structure of the linear bushing. This is a linear motion system with which cylindrical shaft can smoothly move along the axis. Because there are precise balls inside linear bushing, it can accurately guide the position of the shaft without causing too much friction. For example, in the case of LMK 10 (the inscribed circle diameter is 10 mm), the tolerance is zero to minus 9 μm. In the assembly procedures, we fix position of jigs by penetrating a precise shaft into the linear bushings attached on both jigs.

5.3 Detailed procedures

In this section, we explain the procedures with illustrating pictures.

Figure 5.3: Photograph of linear bushing. This type has flange. (LMK series by THK CO., LTD) [13].

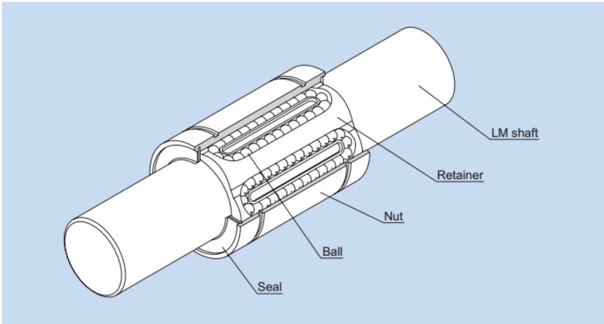

Figure 5.4: Internal structure of linear bushing [14].

5.3.1 Common procedures

The assembly of the ladder begins by preparations of five DSSDs. In this step, we glue PA1 and PA2 with three DSSDs and bond wires between PAs and p-side strips, before five DSSDs are placed on the *assembly-bench* with *DSSD-jig*. Figure. 5.5 shows the situation of the preparation.

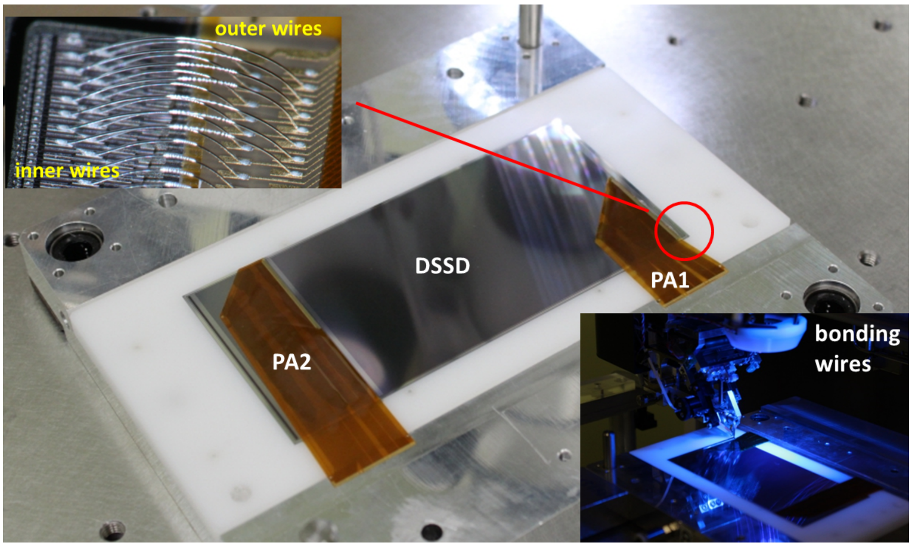

Figure 5.5: Preparation for one DSSD module. After gluing two PAs with DSSDs, we bond wires between p-side strips and PAs. 768 strips are divided by two routes and separately read out by PA1 and PA2.

As the next step, we align five DSSDs on *Coordinate measuring machine* (CMM) with using *xyzθ-stage*. Because jigs fix the relative position of DSSDs in the following procedures, this step is just last one which determines the alignment quality of a finished ladder. Therefore, we must assure sufficient precision. Since this is the most important topic of this thesis, we will explain the details in Chapter 6.

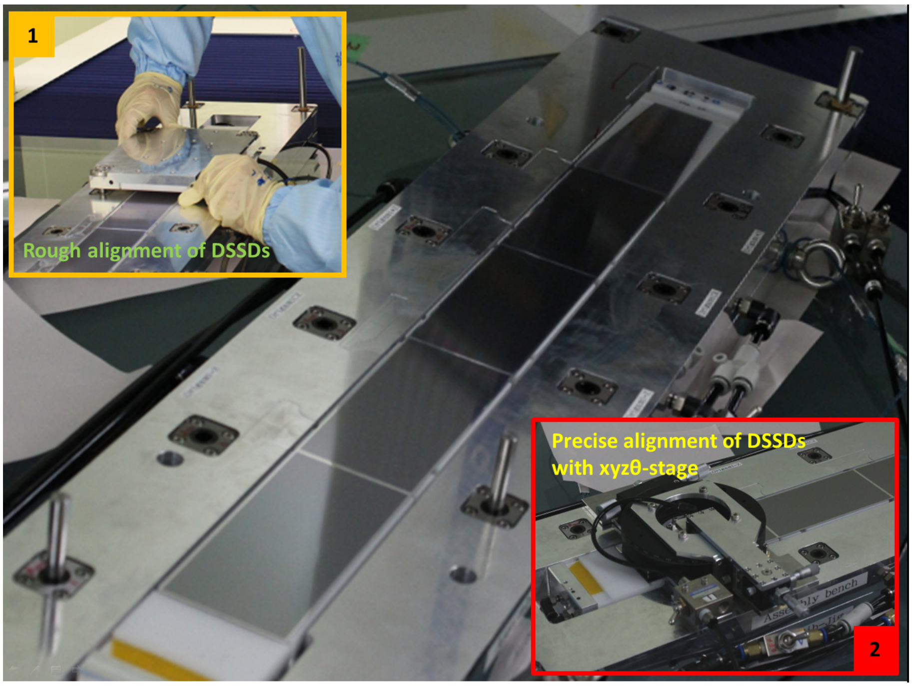

Figure 5.6: First, we roughly align DSSDs by using the *DSSD-jig* on the *assembly bench*. At this stage, the alignment precision of DSSDs are determined by a mechanical precision of jigs ~O(100 μm). Therefore, after putting DSSDs, we perform precise alignment of DSSDs. With this procedures, the spatial error becomes less than 10 μm.

5.3.2 Origami module assembly

For three aligned DSSDs positioned at center, we glue Airex and Origami with DSSDs on the *assembly-bench*. Here alignment jigs developed for Airex sheet and Origami determine their position. Although the requirement of precision of these boards is not severe, we have prepared jigs for each board, because sufficient quality of the alignment offers high quality of gluing which in turn leads to a stable yield of bonding.[1] After waiting for the glue curing, we bond wires between n-side strips and Origami.

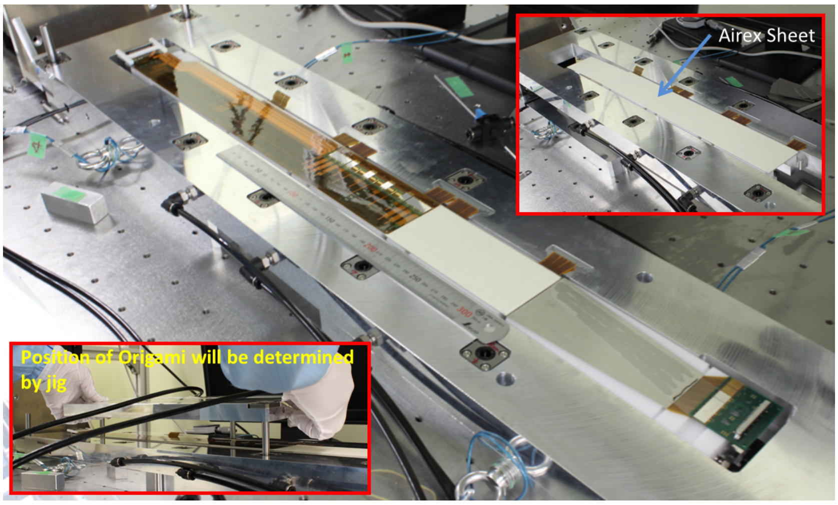

Figure 5.7: Gluing of Origami. After gluing an Airex with DSSDs, Origami is glued. Both boards are fixed by special jigs.

Once we have finished gluing Airex and Origamis, subsequent step is to wrap and glue PAs. This is the most difficult part in an assembly of the ladder since the quality of gluing here largely affects a yield of bonded wires on PAs. Furthermore, there is a chance that we accidentally hit wires bonded between n-side strips and Origamis. In order to reduce operators' burden, therefore, we developed *wrapping-jig* shown in Fig. 5.8. A head of this jig can grab PA1 or PA2 and move them horizontally as well as vertically. Slow movement of this jig enables us to safely wrap and glue PAs.

[1]For more information about gluing and bonding, see Section 5.4 and 5.5

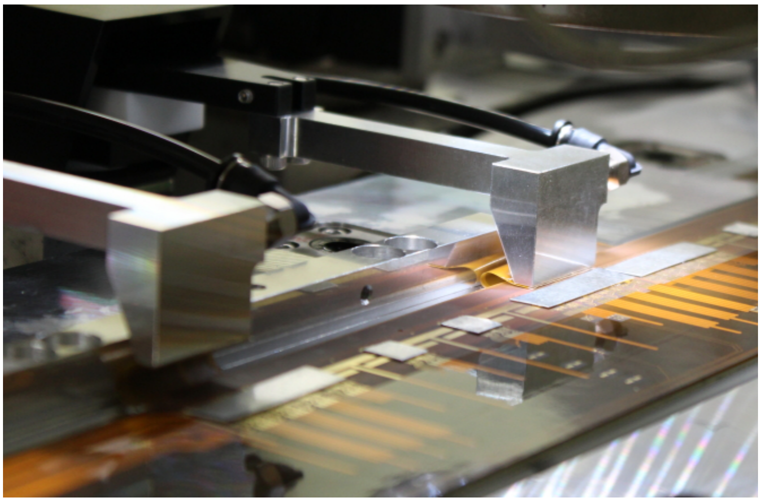

Figure 5.8: The heads of *wrapping-jigs* can grab and move PAs by vacuum chucking.

5.3.3 Assembly of forward and backward module

Forward and backward modules are assembled independently from Origami module. Figure 5.9 shows the procedure of the forward module assembly. There are specialized jigs for every pitch adapters (PF1 and PF2), which allow us to glue and bond wires. The positions of pitch adapters are fixed by pins. Backward module assembly is similar to these procedures.

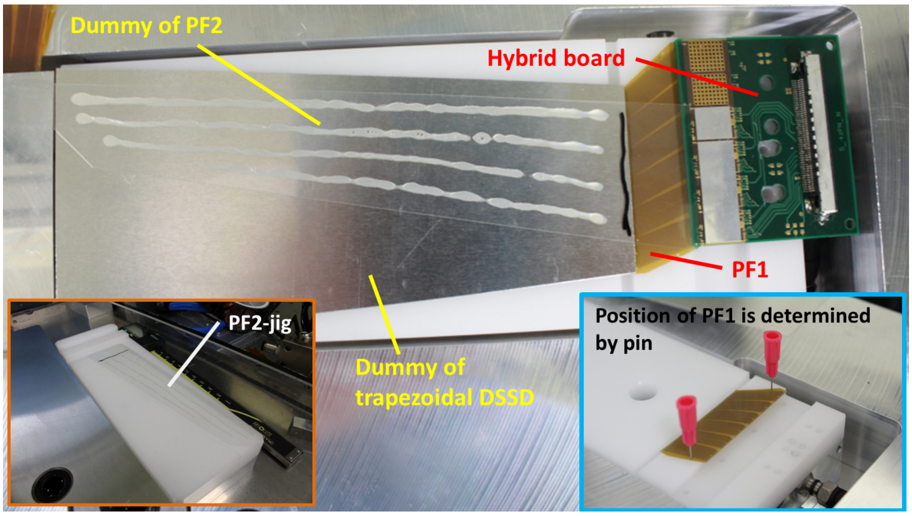

Figure 5.9: Procedure of forward assembly. Because this is the picture during a mockup assembly, we used an aluminum dummy sensor. PF1 and PF2 are positioned by pins on jigs.

5.3.4 Gluing rib and FW & BW modules

Unlike Origami module, forward and backward modules are separately glued with ribs. 3D position of these DSSD is fixed by *slant-jig* and *backward-jig*. These jigs pick up DSSDs from top by vacuum chucking and keep DSSDs into the design position.

5.3.5 Combining rib and Origami module

Finally we combine the rib and Origami module. As Fig. 5.11 shows, Origami module descends to touch glue dispensed on the rib where height of Origami module is fixed at design value by using height stage.

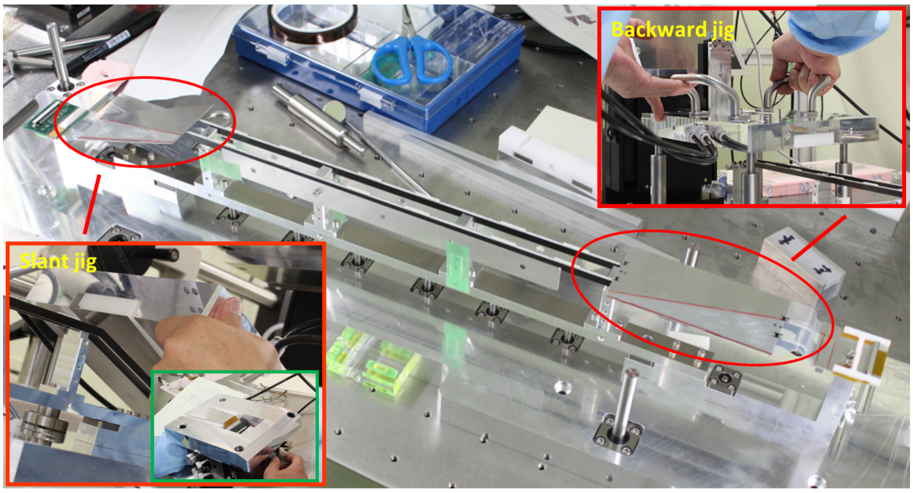

Figure 5.10: Gluing forward and backward modules with ribs are independently done from Origami module. Positioning of forward and backward DSSDs are fixed by *slant-jig* and *backward-jig*.

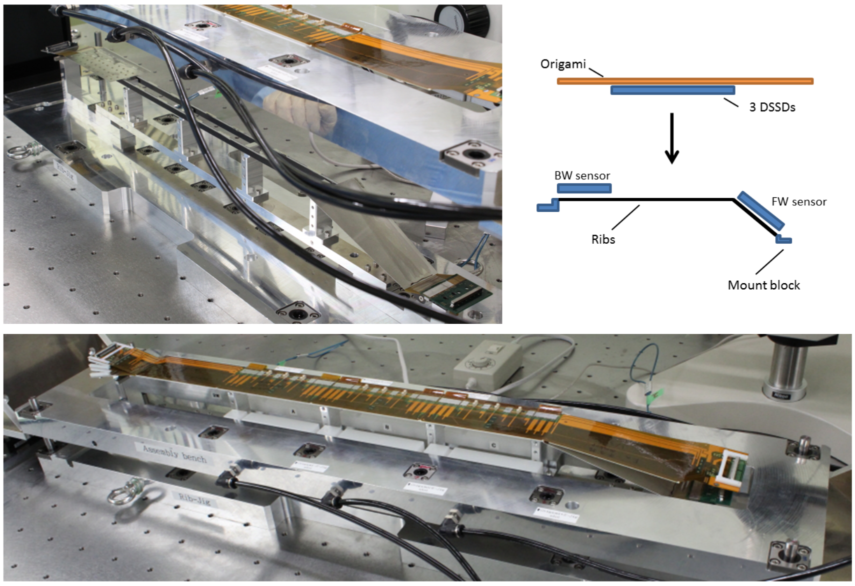

Figure 5.11: After gluing forward and backward modules, we glue Origami module. Height of Origami module is controlled by height stage. We wait for glue to cure before stage starts to descend.

Measurement of the ladder

Figure 5.12 shows a photograph of the finished ladder. Before mounting the ladder on end rings, we measure its mechanical quality: external dimension of the ladder, deformation caused gravity and position of DSSDs. Since there are holes on the surface of Origami, we can observe the position of alignment marks from top. This is a main topic of Chapter 6.

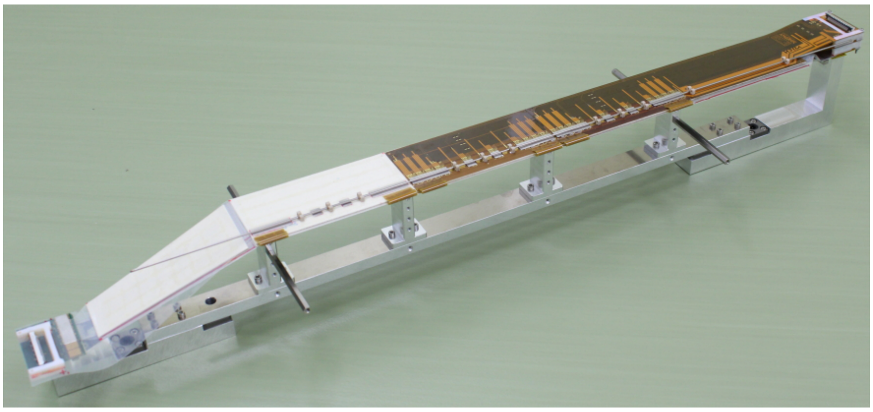

Figure 5.12: Photograph of mockup of finished ladder. Since Origami+z was not ready at taking this picture, a plastic sheet was used as its substitute.

5.4 Bonding

Electrical connection among sensors, flexible board and APV25 chips are done by wire bonding. Of all bonding method, what we adopt is *wedge bonding*. As shown in Fig. 5.13, wedge bonding, the name comes from shape of tools, is the oldest semiconductor assembly process in which metal wire is pressed and vibrated at ultrasonic frequency to form 1st and 2nd bonds. As a bonding wire, we use thin aluminum wire whose diameter is 25 μm. [2] This is one of the thinnest wire in normal commercial use.

Figure 5.14 is an actual picture of bonding between Origami and DSSD (n side). Because there is a difference of height by $\sim$1 mm, the relative position of Origami and DSSD is likely to be misplaced. However, even if there is a misalignment, flexibility of wires can absorb it to some extent.[3] Like the situation shown in Fig. 5.14, dual structure is adopted for most parts in order to reduce wire density.

In order to minimize the necessary time, an optimization of bonding parameters are very important, because it takes considerable time to bond all wires; layer-6 ladder has approximately 15000 of bonding-wires. If optimization of parameter is improper, wire bonding can easily fail and we must repair every failed wire by manual.

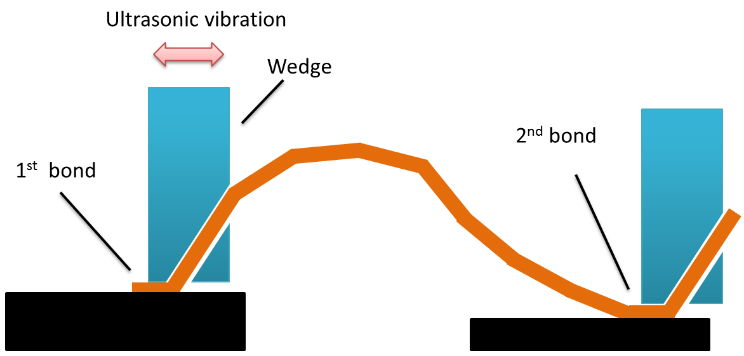

Figure 5.13: Drawing of wedge bonding. At first, tool descends to sample and vibrates at ultrasonic frequency to form initial bond. After the first bond, the tool open its cramp and goes to second position before 2nd bond is formed in a similar way.

[2]In addition to Al, small amount of Si (1%) is contained.

[3]Although it depends on the distance between pads, a few pads of misalignment can be absorbed.

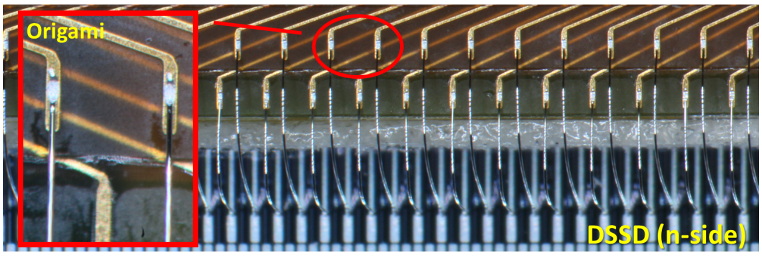

Figure 5.14: Bonding example between Origami and DSSD (n side). This place has the largest difference in height. In order to decrease density of wire, double structure is adopted.

5.5 Gluing

Not only wire bonding but also gluing is important procedure in full ladder assembly. Though gluing does not take longer time compared to bonding wires, it is much more essential for ladder assembly in that quality of gluing largely affects the yield of bonding.

For instance, see Fig. 5.15. Clearly bonding failed on pads underneath which bubble exists. Owing to bubbles, ultrasonic power is dissipated and bonding fails.

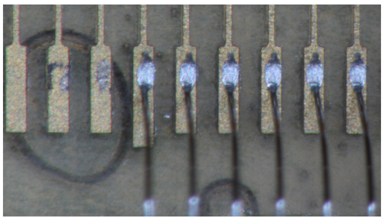

Figure 5.15: Existence of bubbles prevents us from bonding wires correctly. In this case, bubbles occurred during mixing of glue had entered underneath pads. Since it is almost certainly impossible to bond wires on these pads, we must avoid entering bubbles especially for some important pads such as ones connected to bias voltage lines of sensor.

As a material of glue, we use *Araldite 2012*. (Fig. 5.16) This is the two component epoxy adhesive which has good stabilities for heat and chemical and is known as a radiation hard adhesive in the high energy physics experiments. It is not until mixing resin and hardener that the glue starts to cure. In order to assure the same ratio between resin and hardener and prevent bubbles, we use specialized gun and mixer.

Figure 5.16: Epoxy adhesive named *Araldite 2012*. Because of its specification and high reliability, this is often used for leading-edge industry [15].

Additionally, it is inevitable to uniformly and safely dispense glue on samples especially under bonding pads. After a lot of experiments to try manual dispensing, we concluded to give up using our hands and to adopt gluing robot. Fig. 5.17 is a picture of the robot. Once we teach the rule of movement of nozzle, robot automatically follows the command.

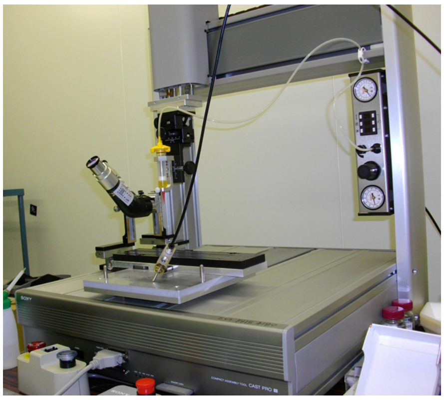

Figure 5.17: Automatic robot and glue dispenser, SONY CAST-PROII. By teaching program in advance, movement of nozzle and timing of compressor can be automatically controlled.

So as to achieve high bonding yield,

- no existence of bubbles underneath the bonding pads
- no overflow from edge
- uniformity of thickness

are required. Of course, minimum amount of glue should be maintained to assure sufficient adhesive strength.

As an example of gluing, we take gluing between PAs and DSSD. (See Fig. 5.18.) During these procedures, position of sensor and PAs are fixed by jig, which enables us to safely glue them with keeping reproducibility.

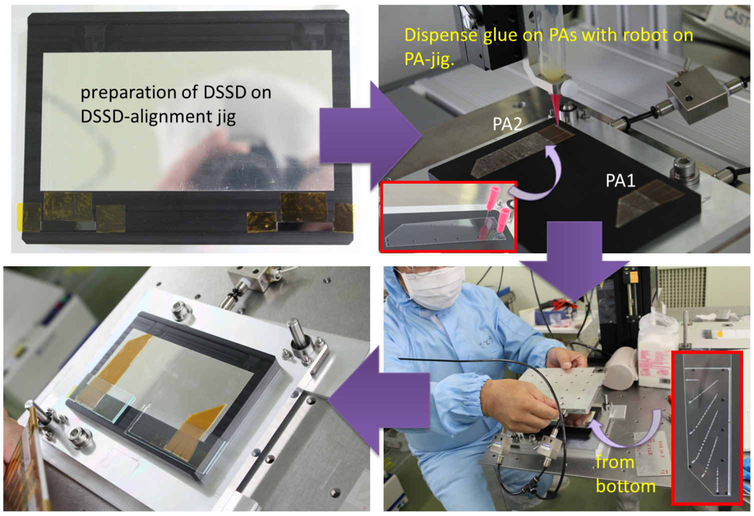

Figure 5.18: Gluing procedure between PAs and DSSD. First of all, DSSDs are roughly aligned on jig using alignment bumps. Two PAs are also aligned on *PA-jig* using alignment holes. For fixed PAs, gluing robot automatically dispenses glue according to the pattern which was taught in advance. Kept by vacuum chucking, PAs are glued with DSSD.

Chapter 6

Mechanical QC/QA

Since SVD is a detector which measures the position of decaying particle, it should be assembled within a certain alignment precision. In order to improve the quality, we actively move DSSDs into appropriate positions. On the other hand, we must measure and assure the displacement of DSSDs in the finished ladder after assembly. These processes are called Quality Control (QC) and Quality Assurance (QA). In this chapter, we explain details about the QC/QA.

6.1 Requirement for mechanical quality control

The alignment qualities of innermost and outermost layer are relatively sensitive to the impact parameter resolution compared to other layers. Figure 6.1 shows a conceptual drawing of reconstruction of the vertex. The closer (the farther) innermost (outermost) is placed, the more accurately position of the vertex is reconstructed. This means that innermost and outermost layer have relatively higher contribution to the impact parameter resolution. Especially as for layer-6 ladder, in spite of its difficulty in alignment (this comes from its size), the requirement of precision is relatively severe.

Based on the above requirement, we decided that our goal was 10 μm as a precision of the initial alignment in flat plane. Here the meaning of an alignment precision is an acceptable error from design value in *ladder coordinate system.* [1]

[1]Of course it may be better if we can align DSSDs more precisely than this number. However, owing to a shift of an exchange of samples between jigs, excessive higher value in itself does not make sense. Furthermore, it takes additional time to overcome higher quality in alignment. This value was decided by considering not only demand of physics

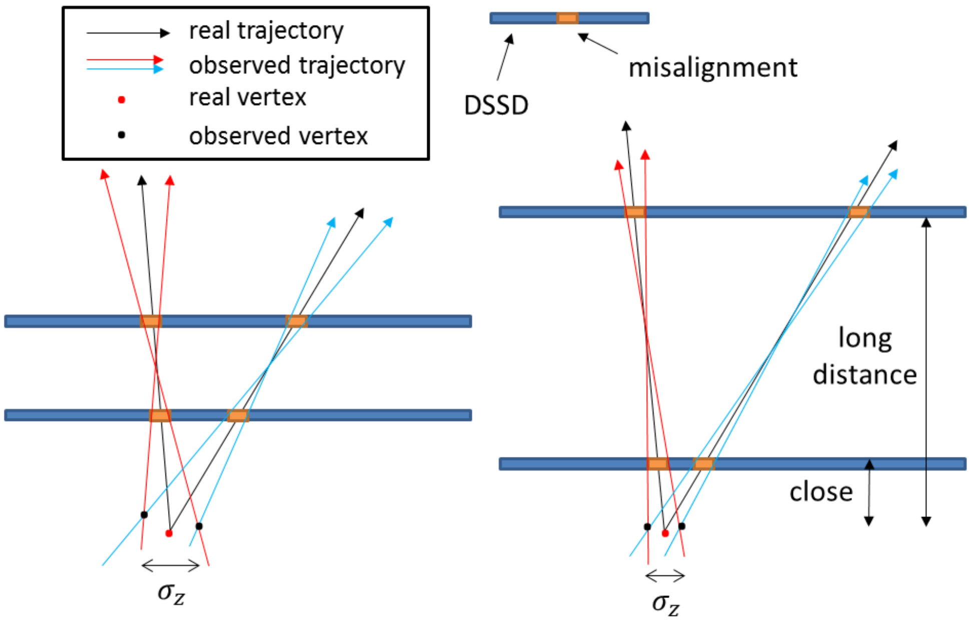

Figure 6.1: Conceptual drawing of vertex reconstruction. Due to misalignment of DSSDs, the observed trajectories are incorrectly determined. The error is, however, minimized if the innermost or outermost layer is placed closer to (far from) vertex.

6.2 Flow of mechanical QC/QA

Fig. 6.2 shows a flow of mechanical QC and QA. Basically mechanical QC/QA are divided into two procedures. At an initial stage of assembly, we perform QC where DSSDs are precisely aligned in flat plane. Since the relative positions of DSSDs from origin point are fixed in the following procedures, we expect that initial alignment keeps until we finish the ladder.

Once we finish assembling ladders, we evaluate mechanical precision (QA). Here not only the position of DSSDs but also sag caused by gravity and external dimensions are measured. Above information is stored into a database and utilized in physics analysis.

but also time efficiency in assembly.

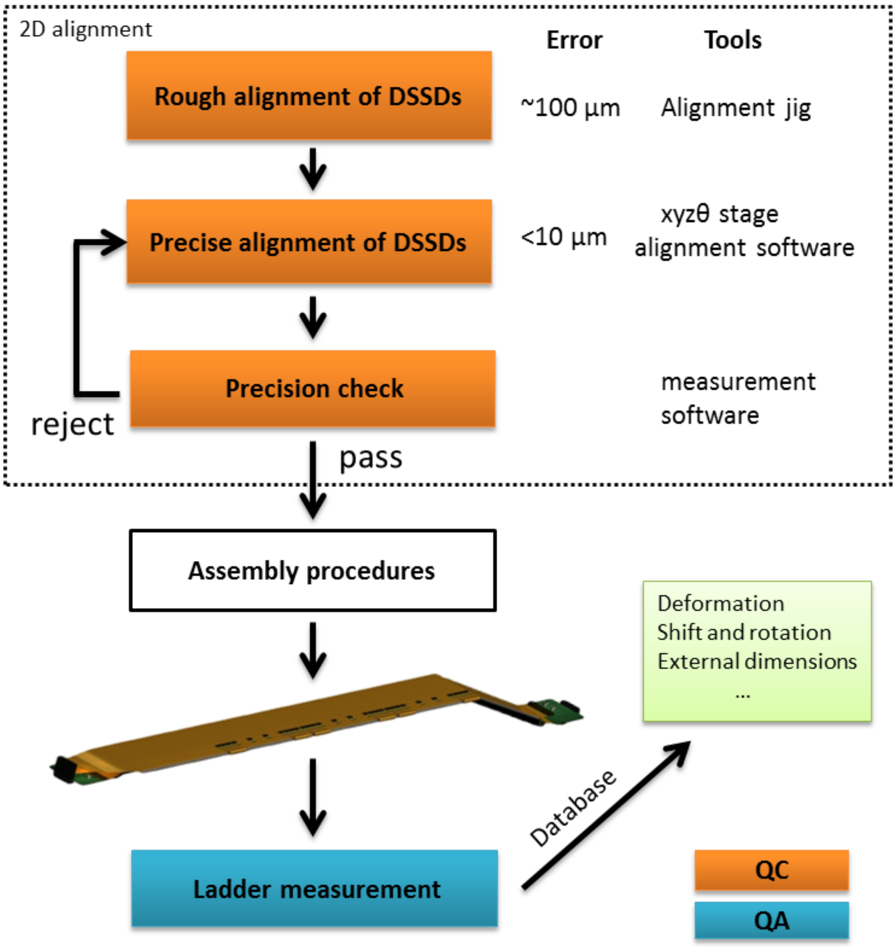

Figure 6.2: Flow of procedures relevant to mechanical quality management. We roughly place DSSDs on jig before precise alignment is done on CMM. If the precision surpasses our criteria in following check, precise alignment is performed again.

6.3 Coordinate system of ladder

In order to perform the mechanical QC/QA, we must unify a definition of ladder coordinate system. In this section, we explain the definition and usage of the system.

6.3.1 Definition of the coordinate system in ladder

In order to determine the coordinate system, we use two holes of the *mount blocks*. As a direction of z axis, we use a vector formed by two holes pointing from backward to forward. For a next axis, we use plane of DSSD. This means that y axis is a normal vector of the plane. x axis is naturally determined by using y and z axises: $\vec{x} \equiv \vec{z} \times \vec{y}$. The origin of these axises is center of backward hole, where $y = 0$ is the height of bottom surface of *mount block*. The situation is shown in Fig. 6.3

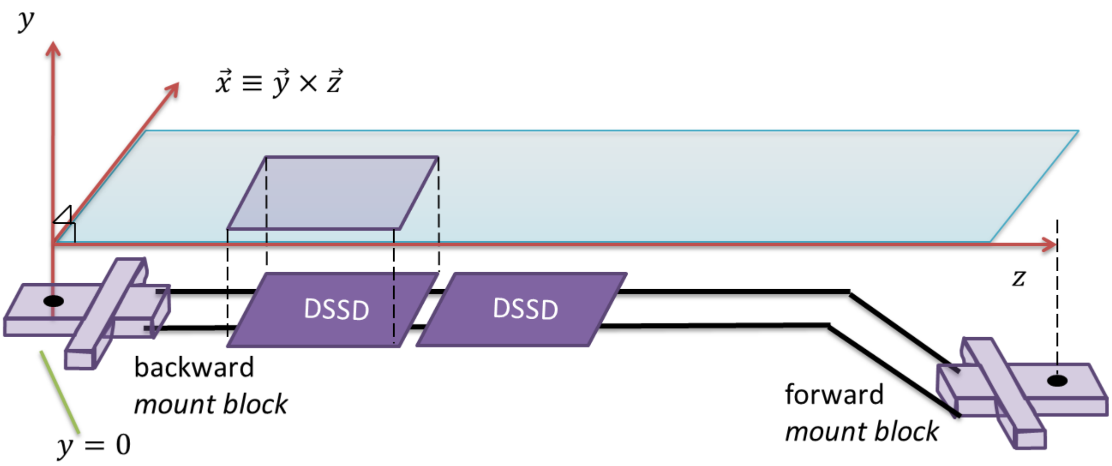

Figure 6.3: Definition of coordinate system of ladder. The center of holes of *mount block* and a surface of DSSDs define the coordinate system.

6.3.2 Determination of the ladder coordinate system in assembly

In order to practically determine the coordinate system of ladder, we use coordinate measuring machine (CMM) (Mitsutoyo QV-X606P1L-C). Figure 6.4 is a picture and control window of CMM. CMM is a measuring instrument which enables us to know 3D position of objects by focusing optically special lens whose depth of field is very small. 3D position of a sample is easily obtained. The measurement precision is summarized in Table 6.1. Since the length of layer-6 ladder is ∼650 mm, we can measure the position of objects with an accuracy of $1.5 + 3 \times 650/1000 \sim 3.5$ μm over whole region. We attached the more detailed specification of CMM in Appendix D.2.

[2]L is in mm.

Table 6.1: Precision of coordinate measuring machine

Direction	Value
Horizontally	(1.5+3L/1000) μm [2]
Vertically	(1.5+4L/1000) μm

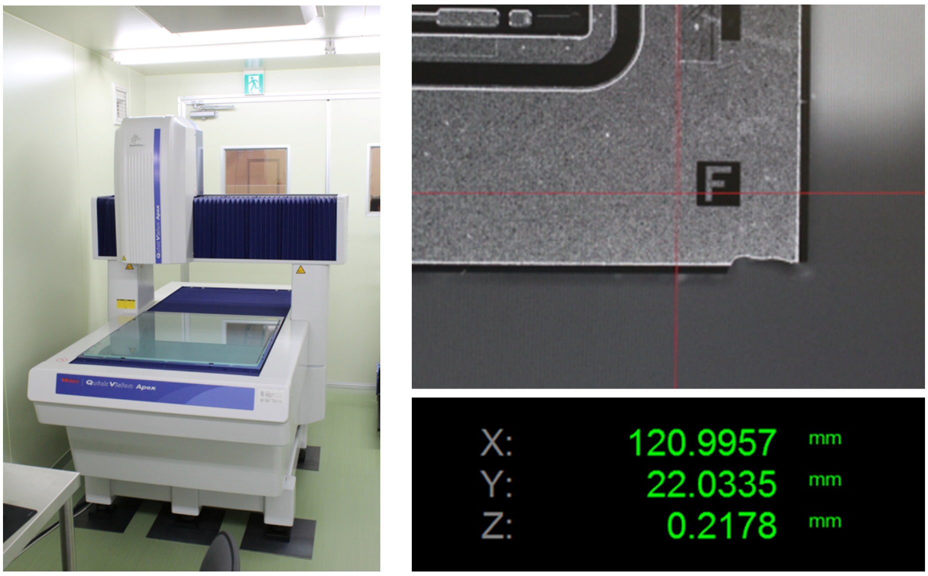

(a) (b)

Figure 6.4: Picture of CMM (Mitsutoyo QV-X606P1L-C)(a). Number of X, Y, Z represent the position of red crossed hair (b).

In the assembly of ladders, we define the ladder coordinate system by using holes of *rib-jigs*, which are located at both ends of *assembly-bench* and play roles in supporting *mount blocks*. Figure 6.5 is photographs of the backward *rib-jig*. By penetrating a precise pin into holes, we fix whole structure of the ladder. Therefore, we expect that the horizontal positions of the center of these holes are equivalent.

As a surface of DSSDs, we use the surface of *assembly-bench*. By fitting points on the surface of *assembly-bench* to plane, we can define y axis. However, an actual measurement suggests that we do not need to consider the gradient of *assembly bench* in the initial alignment. We measured the angle χ shown in Fig. 6.6a, angle formed by two normal vectors of surface of *assembly-bench* and base of CMM to be 0.3 mrad. Therefore, as shown in Fig. 6.6b,

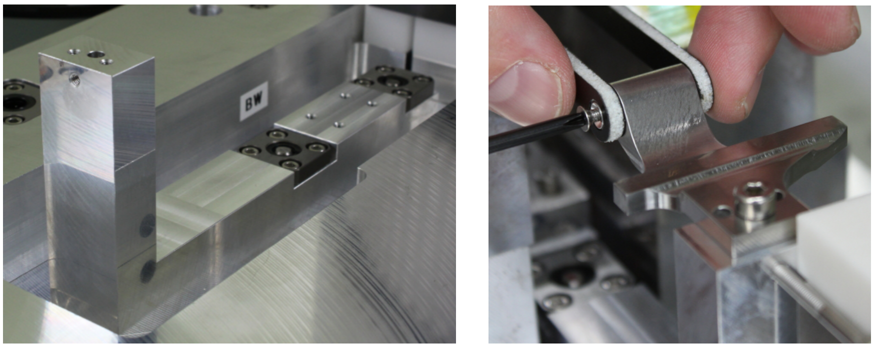

(a) (b)

Figure 6.5: The *rib-jig* (a). We use this hole for the definition of Coordinate in assembly. This jig supports *mount block* by penetrating a pin (b). When we took the picture 6.5b, we substituted a screw for the precise pin.

even if we align DSSDs with respect to a certain place of an alignment mark, displacement of another alignment mark Δ is only $\Delta = L \times (1 - \chi^2/2) \sim 9$ pm. Here we used $L = 120$ mm as a distance of a longer side of DSSD. Thus in the initial alignment of DSSDs, we can use vertical axis of CMM as a definition of y axis, where we use the surface of the *rib-jig* as a zero level of y axis. These definitions is drawn in Fig. 6.7.

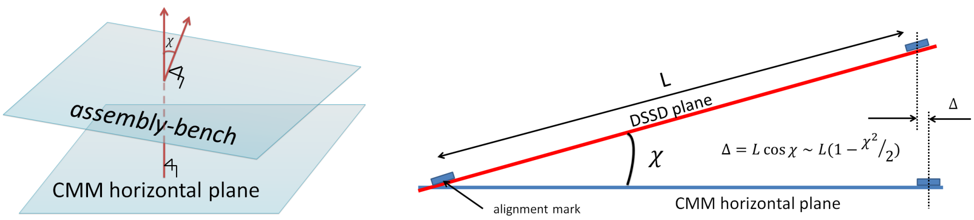

(a) (b)

Figure 6.6: The angle χ is defined as an angle between normal vector of *assembly-bench* and that of CMM-horizontal plane (a). If we align DSSD with respect to a left alignment mark, displacement of a right alignment mark caused by the relative gradient of plane becomes $L \times (1 - \chi^2/2)$ (b).

So as to use the holes as a definition of the ladder coordinate system, we must locate a position much more precisely than our goal 10 μm. Although the radius of the hole is much larger than our aim, it is possible to locate the center of hole by fitting points on an edge of holes. As Fig. 6.8 shows, CMM can simultaneously detect multiple points with edge pattern recognition and

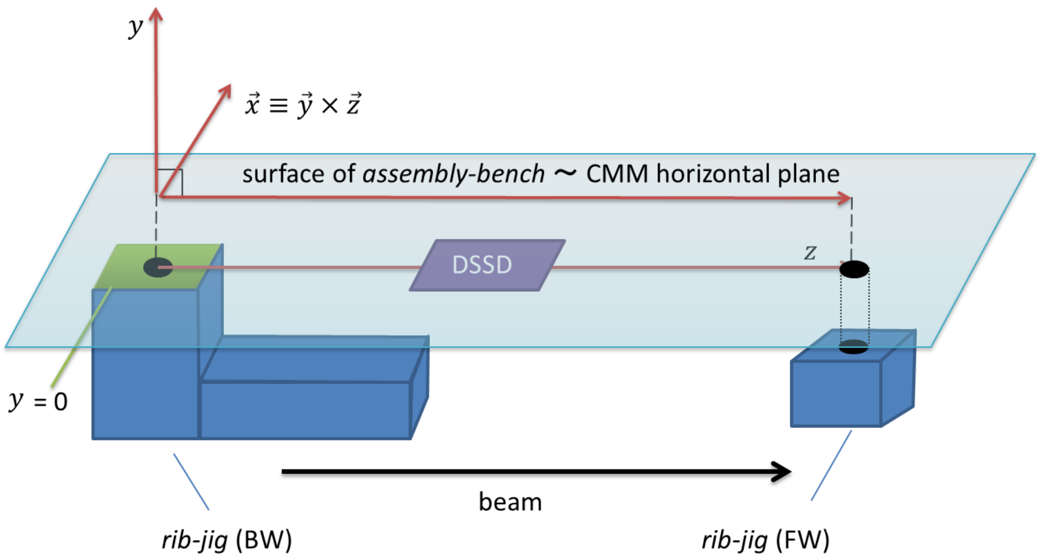

Figure 6.7: Practical way to determine the coordinate system of ladder. First, we measure the center of holes of the *rib-jigs*. These holes can be used to define the horizontal origin and direction of z axis. Second, we use vertical axis of CMM as a direction of y. Therefore, direction of x axis result in a cross product of $\vec{y}$ and $\vec{z}$.

enables us to get more than 300 points along with the circumference of holes in the *rib-jig* within approximately 30 seconds. By fitting these large number of points to a circle, we can calculate a location of center with high precision. Figure 6.9 is a scattering plot of the center of hole whose diameter is 3.4 mm. The standard deviation in z and x direction was 0.8 μm and 0.6 μm respectively. This shows that there is a validity to directly use relatively large holes to define coordinate system of ladder.

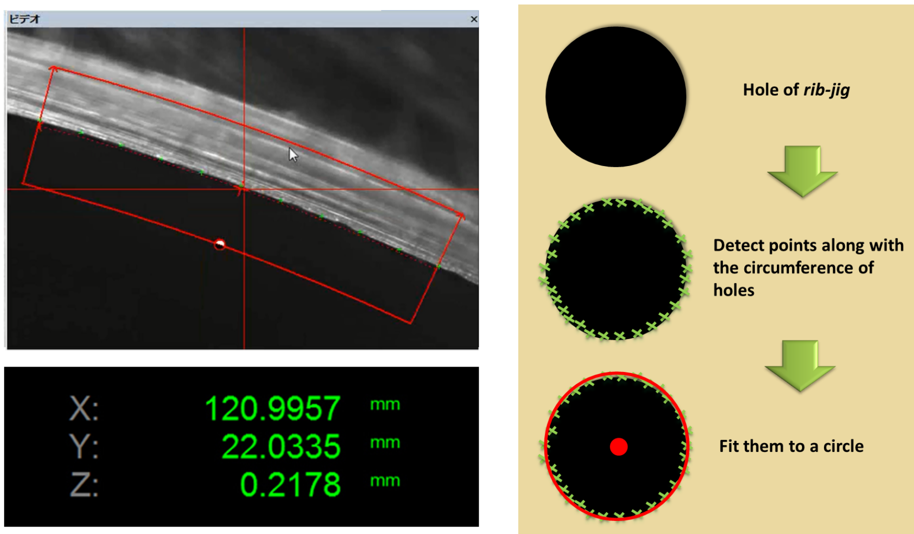

(a) (b)

Figure 6.8: Position of hole can be extracted by fitting points. Green dots represent the detected points.

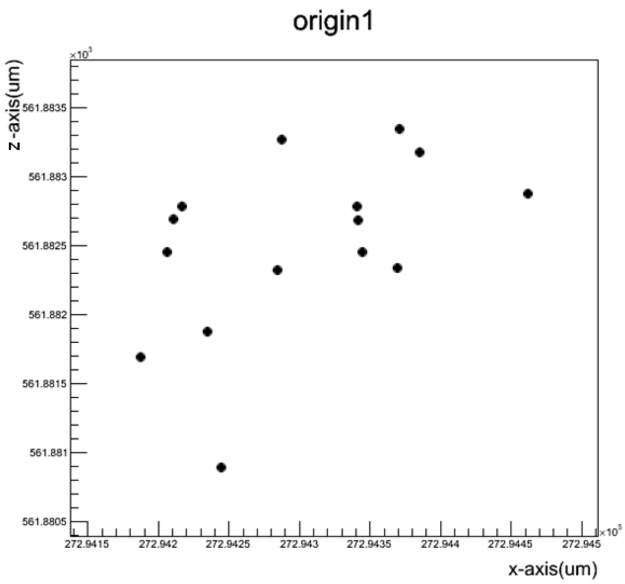

Figure 6.9: Scattering of measured position of center of hole. The standard deviation was $\sigma_x = 0.8$ μm and $\sigma_z = 0.6$ μ m. This is enough precise to use holes so as to define coordinate system of ladder.

6.4 Coordinate system of DSSD

We must also define coordinate system of DSSDs. As a definition of two axises, we choose the same directions as the ladder coordinate system: direction of n-side pitches for z axis and p-side pitches for x axis. On the other hand, position of horizontal origin O_d depends on the kinds of DSSDs. Since strips of the rectangle DSSDs have their own numbers before shipment, we use an intersect point of both No.0 strips. Although strips of trapezoidal DSSD also have the numbers, we do not use the intersect point for a reason of design. Instead we use a forward edge of No.0 p strip as a definition of O_d. These are summarized in Fig. 6.10. From here on, we promise to use a superscript letter with a star to represent a component defined in DSSD coordinate system.

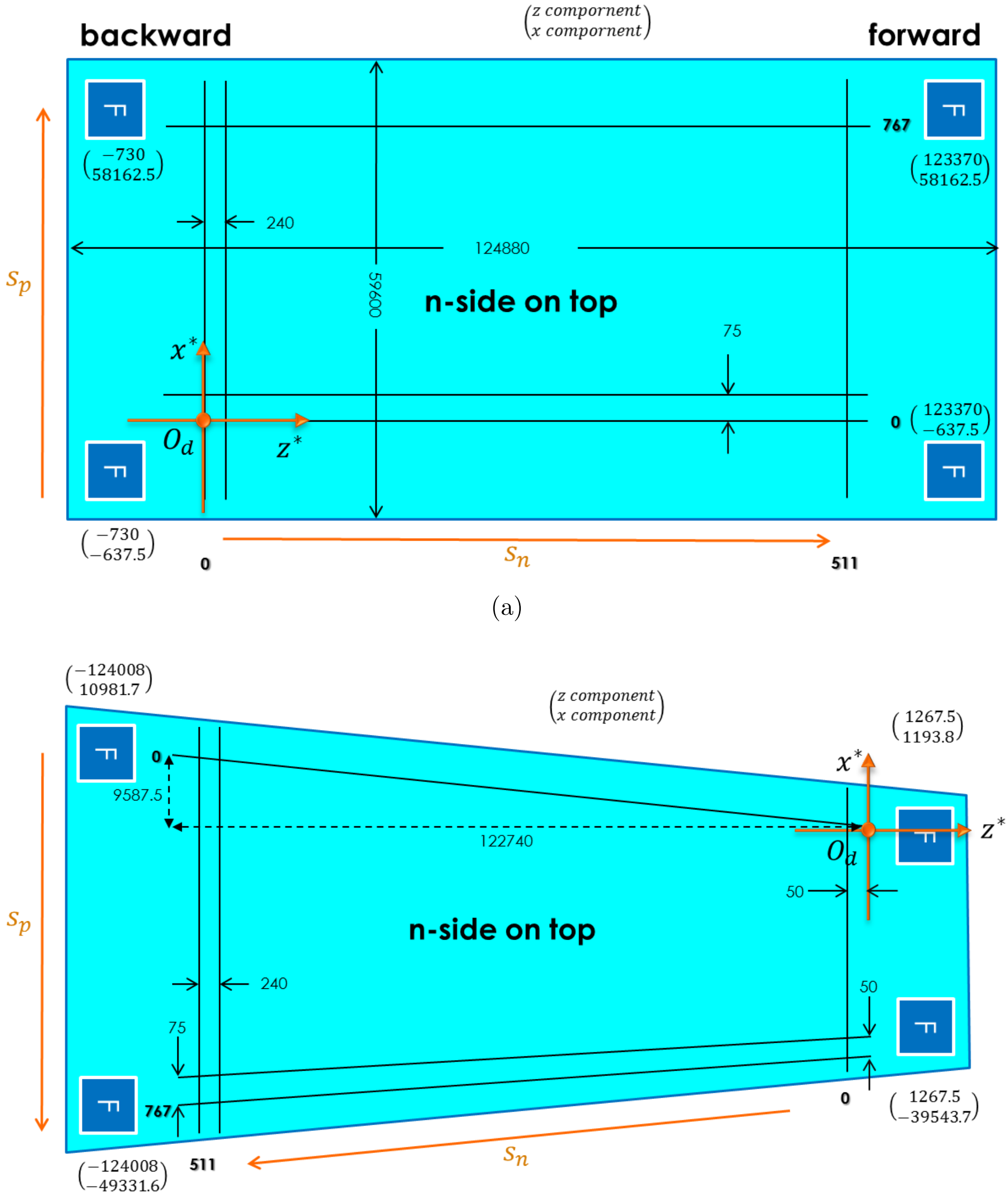

(a)

(b)

Figure 6.10: Definition of the coordinate system of large rectangle DSSD (a) and trapezoidal DSSD (b). S_p and S_n represent the suffix of strips. Two numbers in parenthesis are places of alignment marks in this system. A unit of all numbers is μm.

6.5 Measurement of DSSDs' position

In order to align DSSDs, we must prepare a method to measure the position of DSSD. Otherwise we are not able to judge whether our alignment succeeded or not. *Alignment marks* made by photolithography at the corners of DSSDs are very precisely positioned and used to measure the misalignment. As Fig. 6.11, for every side of an alignment mark, we get points by detecting change of contrast and fit them to lines. Two intersect points obtained from these lines are used to calculate the position of the center of an alignment mark. Again, sufficient precision is required to achieve appropriate measurement. Since our goal of alignment error is 10 μm, we must measure the position with precision much better than this number.

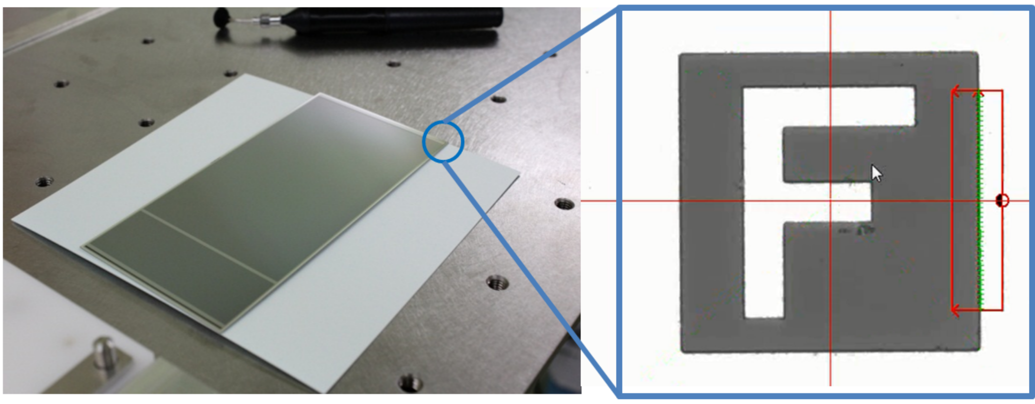

Figure 6.11: Alignment mark is made at the corner of DSSD. Conventionally the letter F is often used for Hamamatsu's DSSD in order to avoid freedom of rotation.

Figure 6.12 and Table 6.2 show the result of reproducibility test for four corner of DSSD. The obtained reproducibility was better than 1 μm, and we conclude that the precision of measurement of alignment mark is sufficient for the mechanical QC/QA.

Once we are able to get positions of four alignment marks, we must convert these data into some parameters which represent displacement of DSSD. We adopt three deviation parameters to represent the translation and rotation of DSSD from design value: $\Delta z, \Delta x$ and $\Delta\theta^{\star}$. As Fig. 6.13 shows, $\Delta z, \Delta x$ represent a translation of origin point from design value in ladder coordinate system and $\Delta\theta^{\star}$ a rotational angle around the origin point of DSSD (O_d).

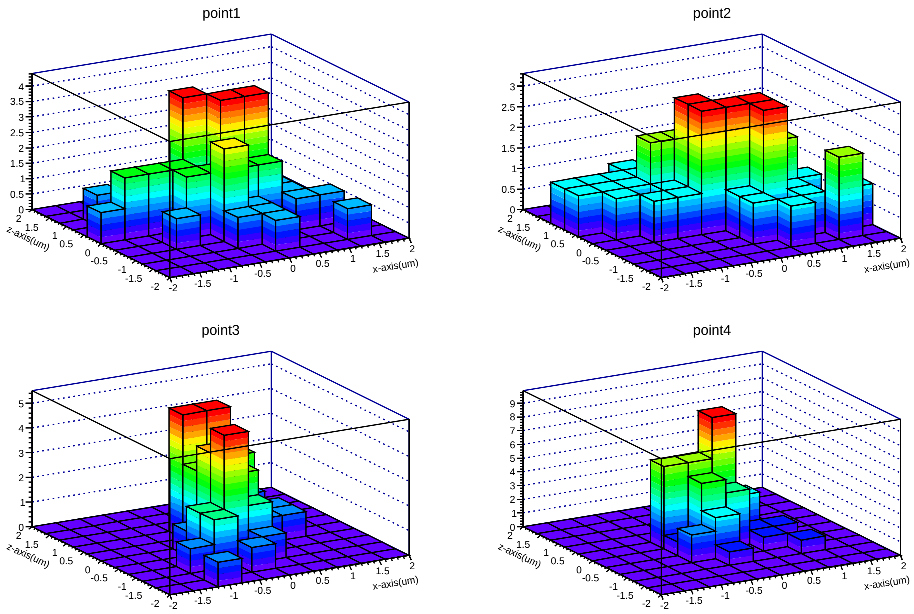

Figure 6.12: Distribution of positions of alignment marks. The horizontal value means difference from average. The point1 to point4 correspond to the four corner of the alignment marks. The definition of point will be shown in Fig 7.5. Number of entries is fifty.

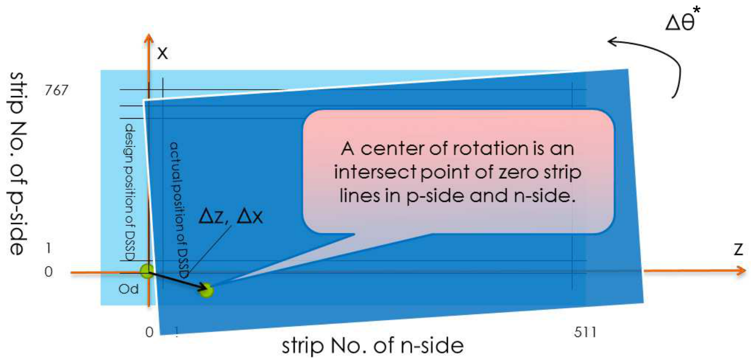

Figure 6.13: Definition of deviation parameters. $\Delta z, \Delta x$ represent a translation of origin from design value. $\Delta\theta^{\star}$ represents a rotation angle of DSSD around origin point.

These deviation parameters are obtained by minimizing χ^2 value defined as following formula.

Table 6.2: Standard deviation of measurement of alignment marks for each corner.

Point	σ_X (μ m)	σ_Y (μ m)
1	0.7	0.5
2	0.8	0.7
3	0.4	0.7
4	0.4	0.4

$$\chi^2 = \sum_{\text{point}:i=1,2,3,4} \frac{\left[r_i^\star \cos\left(\theta^\star_{i;\text{design}} + \Delta\theta^\star\right) + \Delta z + z_{O_d;\text{design}} - z_{i;\text{measure}}\right]^2}{\sigma^2} + \frac{\left[r_i^\star \sin\left(\theta^\star_{i;\text{design}} + \Delta\theta^\star\right) + \Delta x + x_{O_d;\text{design}} - x_{i;\text{measure}}\right]^2}{\sigma^2}$$

As shown in Fig. 6.14, $r_i^\star$ and $\theta^\star_{i;\text{design}}$ is a distance and angle from O_d. $z_{O_d;\text{design}}$ and $z_{i;\text{measure}}$ or $x_{O_d;\text{design}}$ and $x_{i;\text{measure}}$ represent design and measured value of O_d in ladder coordinate system. As a standard deviation σ, we use specification value of CMM. With this fitting, we can get the horizontal position of O_d and rotation angle with precision approximately 2 μm and 0.3 mrad.

In order to check the goodness of this fitting, we can use χ^2 test. Since the $\chi^2 = 22$ gives 0.95 to its cumulative distribution function with 8 degrees of freedom, we use this value as a significance level of 5%: if $\chi^2 > 22$, we will try the measurement again.

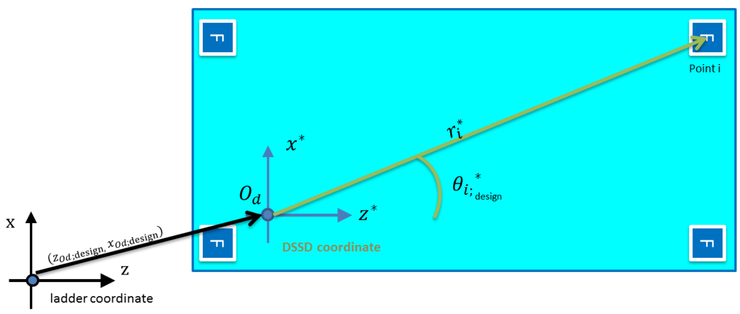

Figure 6.14: Definition of design values. As mentioned in the text, components in DSSD coordinate system have stars.

6.6 Alignment of DSSDs

The precise alignment of DSSDs is performed on CMM by using *xyzθ-stage* and an alignment software developed by ourselves. As illustrated in Fig. 6.15, this jig has a vacuum-chucking pad, which is movable along not only three directions x, y and z but also rotation around y axis. By holding DSSD with this jig, we can translate and rotate DSSD into design position. In order to inform user of the design position, we use the software designed for the layer-6 ladder.

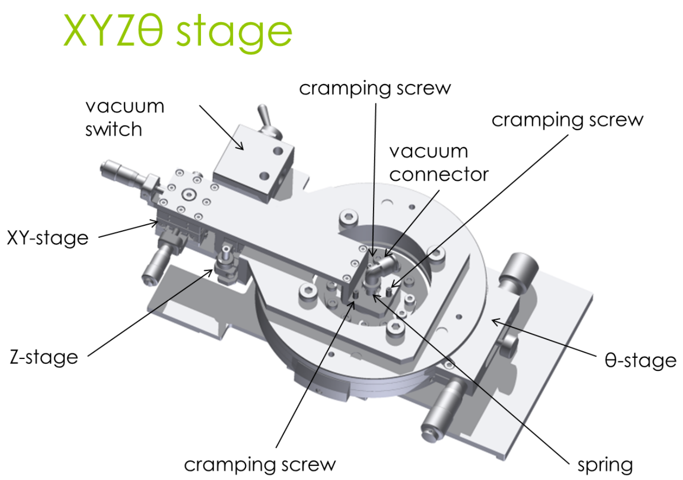

Figure 6.15: *xyzθ-stage*. This stage can hold DSSD and move it. Because the height of this stage is less than working distance of CMM, the camera of CMM never hits to this jig.

Since the location of the jig on CMM changes every time we place it, we must locate positions of the holes in the *rib-jigs* before the precise alignment. We present this step in Fig. 6.16. As an assistance for positioning, we manually teach CMM three points on the edge of the hole in the backward *rib-jig*. By using these points, CMM automatically scans the edge and calculates the center. Repeating the same procedure for forward, CMM can calculate the coordinate system of the ladder: design positions of the alignment marks can be specified.

After teaching the coordinate system of the ladder, we perform rough alignment of DSSD. As Fig. 6.17 shows, we place DSSD with the *DSSD-jig*. At this stage, spatial error of DSSD is determined by a mechanical precision of the jig, and it is about O(100 μm). Therefore, we will move DSSD with respect to design positions of alignment marks pointed by the

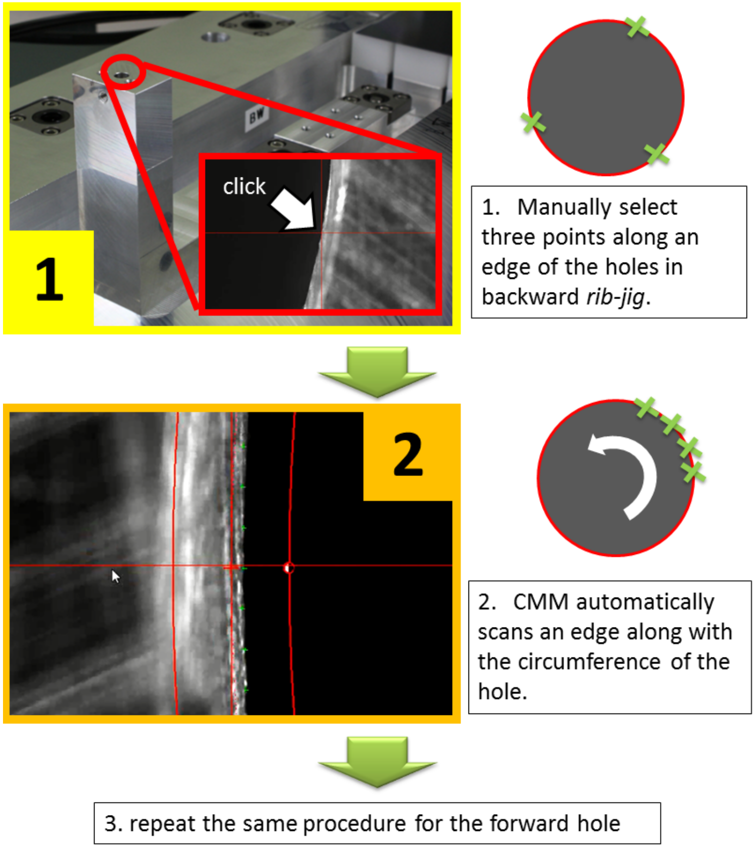

Figure 6.16: Procedure of teaching a location of the hole in the *rib-jig*.

assistant program.

Fig. 6.18 is situation of precise alignment of DSSDs. Once the position of origin holes were measured, one click moves a camera into design position of alignment mark. Since an intersect point of red cross hair is design position of upper-right corner of alignment mark, we will move DSSD with $xyz\theta$-*stage* such that all alignment marks coincide with the design positions.

In order to align all alignment marks constrained one another, we repeat combination of translation and rotation shown in Fig. 6.19. For the purpose of illustration, we call two different alignment marks A and B. First, we translate DSSD such that corner of A coincides with design. Second, we move camera into design position of B. Third, with imagining a perpendicular bisector between B and design point, we rotate DSSD such that B is on the line. Fourth, we return to A. By repeating this procedure, error of translation and rotation will converge. Finally, we check that other alignment marks (C

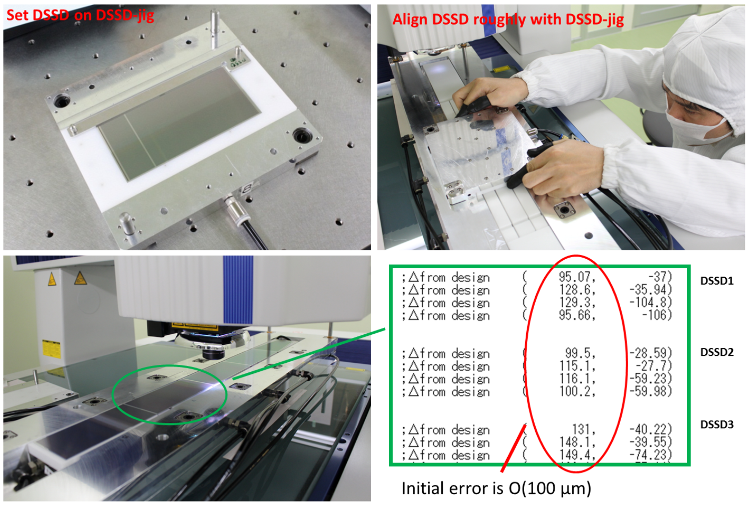

Figure 6.17: First step of alignment of DSSDs. DSSD positioned by *DSSD-jig* is placed on *assembly bench*. The initial error is approximately 100 μm.

and D) are placed in design positions.

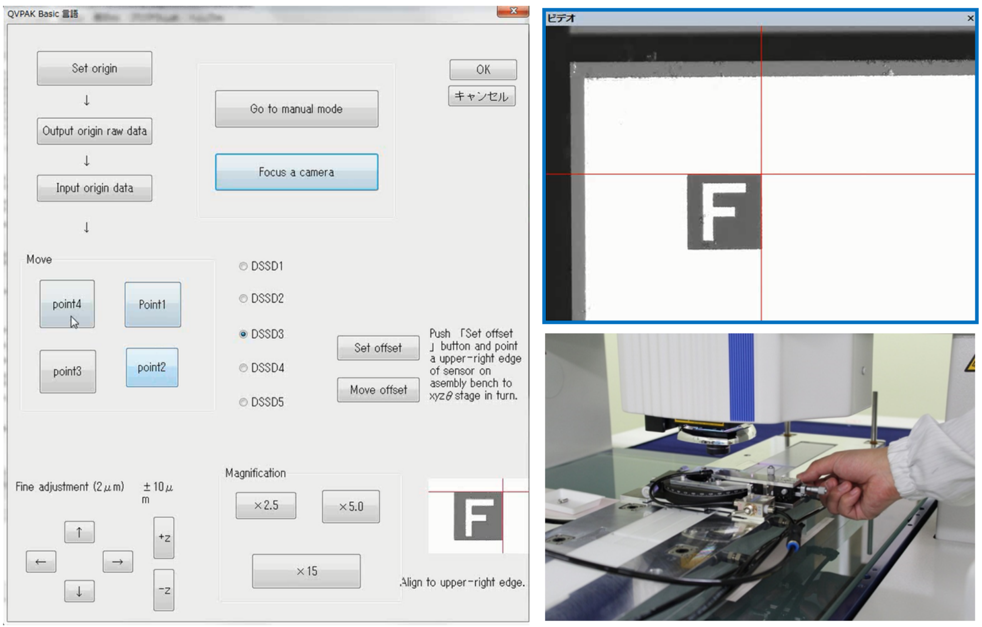

Figure 6.18: Control window of the alignment assist software. Number of DSSDs can be chosen by radio buttons. If you click button named *point1*, a camera of CMM will move to design position of point1. The definition of numbers are shown in Fig. 7.5.

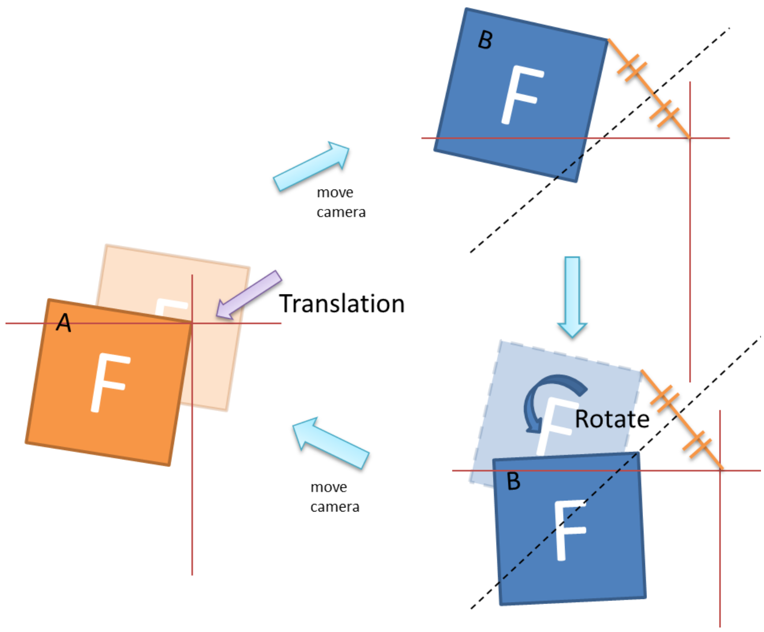

Figure 6.19: Movement of DSSD. In order to converge errors of all alignment marks, translation and rotation must be performed in the proper sequence.

Table 6.3: Result of alignment test.

DSSD [3]	Δx (μm)	Δz (μm)	$\theta^\star$ (rad)	χ^2
1	1.8 ± 2	1.4 ± 2	$(-0.2 \pm 3) \times 10^{-5}$	0.23
2	-3.5 ± 2	1.0 ± 2	$(-0.8 \pm 3) \times 10^{-5}$	0.53
3	-3.4 ± 2	4.2 ± 2	$(3.0 \pm 3) \times 10^{-5}$	0.58

Alignment test

Before a mass production, we tried an alignment test for three DSSD sensors. Figure 6.20 shows the measured positions of alignment marks. This time, just to be safe we tried to measure four times. Since the repeatability of the measurement turned out to be sufficient, we do not plan to repeat four times in real assembly.

Table 6.3 is a result of this trial. The obtained deviation parameters passed our goal 10 μm and the fitting satisfied significance level ($\chi^2 < 22$). Furthermore, the time $\sim$5 minutes needed for an alignment of one DSSD was realistic in assembly of ladders.

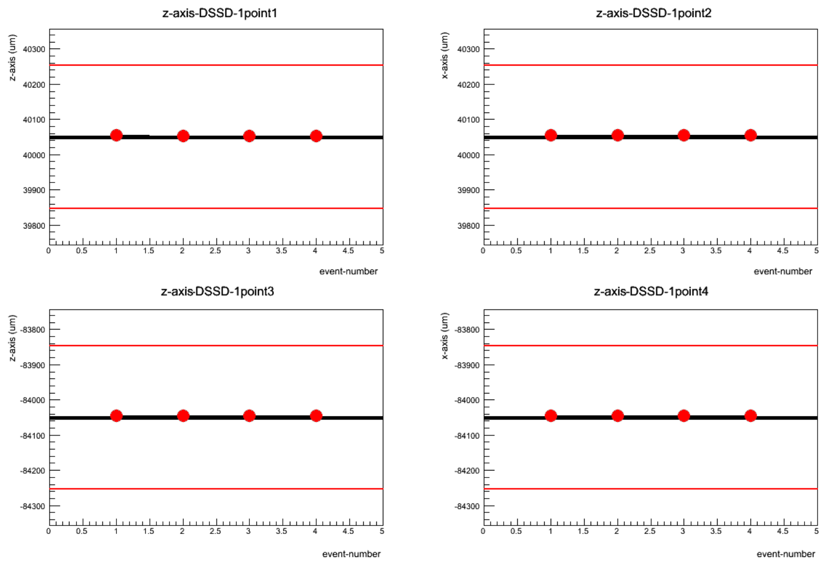

Figure 6.20: Measured position of alignment marks (z component) in DSSD 1. Red and black lines mean acceptable range (10 μm) and design value. Number of point is defined in Fig 7.5.

[3] Number of DSSD will be shown in Fig.7.5.

Chapter 7

Evaluation of alignment precision

As explained in Chapter 5 and 6, the basic procedure of layer-6 ladder assembly was established. As a next step, we evaluate the alignment precision of DSSDs in finished ladder by assembling a mockup. In this chapter, we present remaining issues and future prospects which became clear with this trial.

7.1 Evaluation with mockup assembly

Since we align DSSDs only at the beginning of the assembly procedure, it is important to minimize the translation and rotation of DSSDs during the assembly. Therefore, it is required to verify them by making a mechanical mockup before starting real production of the ladders. Because DSSDs are very expensive, we use dummy aluminum plates instead of DSSDs as a first step of a mockup. Because the dummy aluminum plates do not have alignment marks, we substitute scratches for them. Figure 7.1 shows the dummy aluminum plates and scratches. Preliminary studies suggest that positioning precision of these alignment marks are better than 10 μm.

Along with dummy aluminum plates, there were differences from real ladder. First, we did not align them because the absolute positions of the scratched marks were not precisely determined. What we would like to measure with this mockup was translation and rotation during assembly. Second, we did not attach Origamis, Hybrid boards and Airexes because these components do not affect on the position of DSSDs in principle. This also means that we can omit wire-bonding. If it were not for any translation or rotation of DSSDs during assembly, precision of the DSSDs in the finished ladder

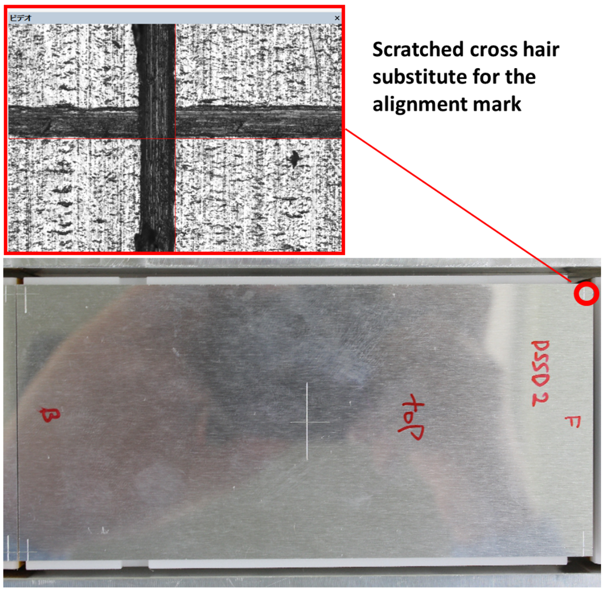

Figure 7.1: Photograph of scratches. These can be used for substitute for alignment marks. In actual measurement, we pointed four corners around the vertex and averaged their positions.

would be error of active alignment. Thus, we can verify the quality of ladder relatively easily and quickly with this simplified mockup.

7.1.1 Assembly of the mockup ladder

The assembly procedures of the mockup ladder is much simpler than real ones. First, we roughly align DSSDs with the *DSSD-jig* in zx plane and measure the position of scratched marks (common procedure). Second, we pick up forward and backward DSSDs with the *Slant-jig* and *Backward-jig* respectively and glue with ribs. Finally, we glue to combine three DSSDs and ribs. These procedures are shown in Fig. 7.2. Third, after the glue cured, we place the three DSSDs to glue on the ribs shown in Fig. 7.3. Then mockup ladder assembly finishes. Because of its simple structure, we could finish the procedures within only two days. Figure 7.4 shows a photograph of mockup ladder.

7.1.2 QA in the ladder assembly procedure

Using the mockup, we measured the position of scratched marks as a QA. Only for this mockup, we did not target the slant DSSD, since it was difficult

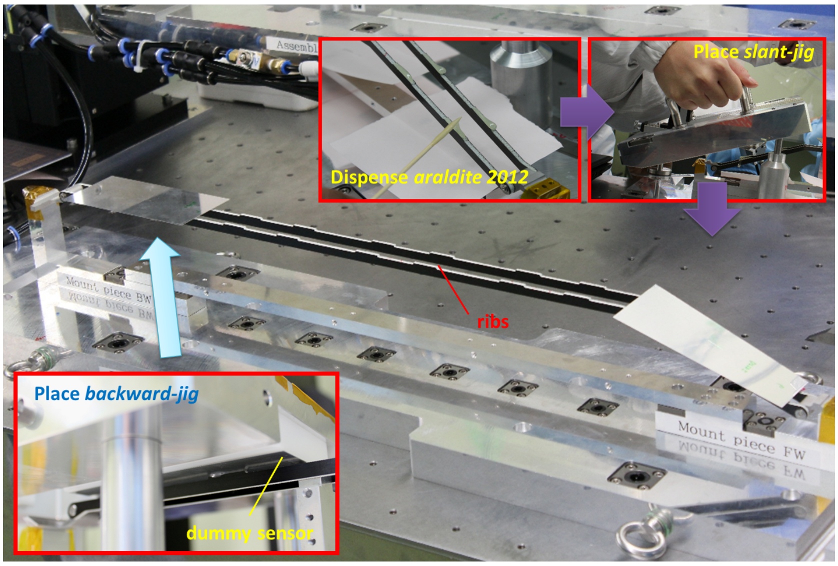

Figure 7.2: Gluing forward and backward DSSDs with ribs.

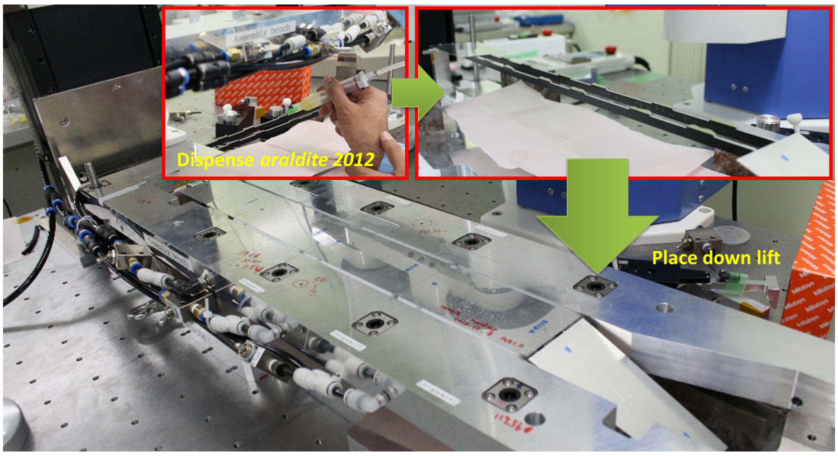

Figure 7.3: Combing three DSSDs and ribs. If we wait for glue curing, the mockup ladder assembly finishes.

to calculate the relation between initial and final position.[1] On the other hand, the translation and rotation of DSSDs in flat regions can be easily calculated by just subtracting initial positions of alignment marks from final ones. The result is summarized in Table 7.1. Here definition of number of DSSD and alignment marks are shown in Fig. 7.5. To make it easy to

[1]In the mass production, we must target a slant DSSD.

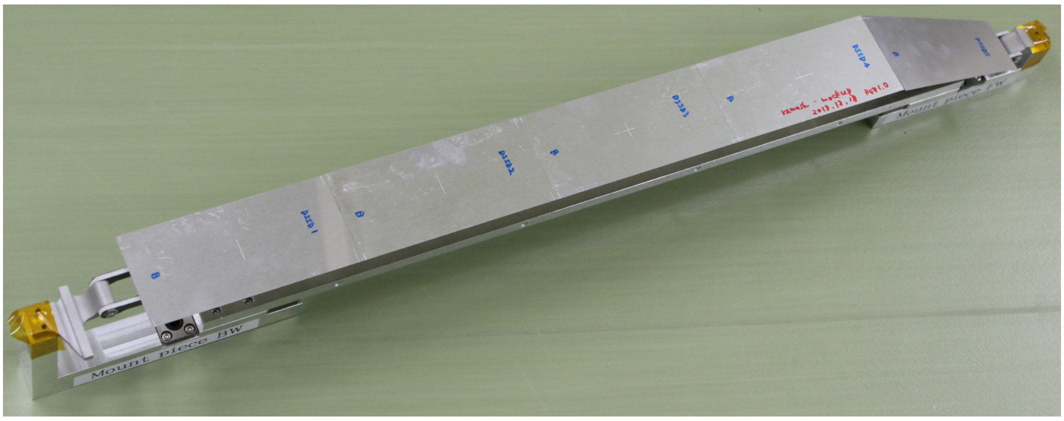

Figure 7.4: Photograph of the finished mockup ladder.

understand, we took a gravity point of DSSD as the center of rotation. As the values shows, the magnitudes of translation were approximately 100 μm along both directions and much larger than the acceptable error of zx plane alignment we had aimed for in active alignment procedure. Although we must distinguish the goals for displacements occurred in the active alignment and during assembly, we should investigate the reasons why these shift had occurred.

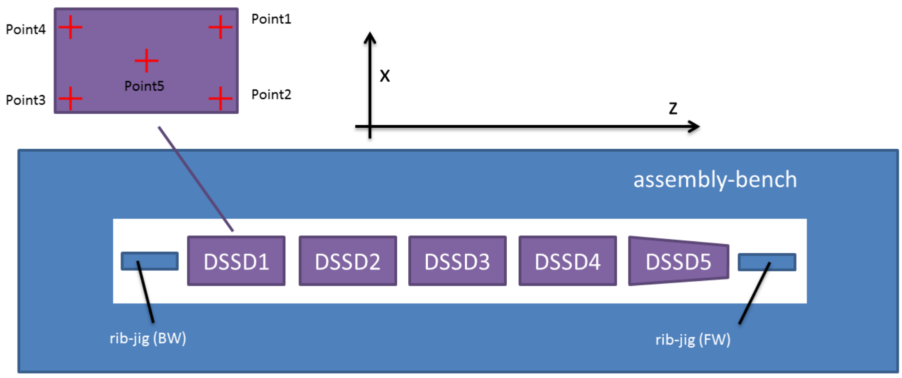

Figure 7.5: Definition of number of DSSD and alignment mark.

Table 7.1: Translation and rotation during assembly

Point	Δx (μm)	Δz (μm)	Point	Δx (μm)	Δz (μm)
DSSD1			DSSD3		
$\Delta\theta^{\star} = (5.9 \pm 0.08) \times 10^{-3}$ (rad)			$\Delta\theta^{\star} = (-4.8 \pm 0.8) \times 10^{-4}$ (rad)		
$\Delta x = -211$ μm, $\Delta z = -21$ μm			$\Delta x = -77$ μm, $\Delta z = 127$ μm		
1	-160	-47	1	-80	126
2	-156	7	2	-81	119
3	-267	6	3	-70	123
4	-269	-45	4	-66	126
5	-211	-21	5	-77	127
DSSD2			DSSD4		
$\Delta\theta^{\star} = (-4.8 \pm 0.8) \times 10^{-4}$ (rad)			$\Delta\theta^{\star} = (-5.3 \pm 0.8) \times 10^{-4}$ (rad)		
$\Delta x = -64$ μm, $\Delta z = 131$ μm			$\Delta x = -86$ μm, $\Delta z = 126$ μm		
1	-64	131	1	-91	126
2	-68	127	2	-92	122
3	-58	126	3	-80	120
4	-57	129	4	-83	126
5	-64	131	5	-86	126

7.2 Possible sources of DSSD displacement

As we saw, translation of DSSDs during assembly was approximately 100 μm along both direction x and z. In these numbers, we can find tendency. Not only the translation but also rotation of DSSD2, DSSD3 and DSSD4 seems to resemble one another. On the other hand, DSSD1 do not. The reason is almost clear because former DSSDs moves equivalently during assembly as a part of Origami module; in principle their relative positions do not change. Therefore, it is natural to guess that the translation ans rotation came from the gaps of linear bushings which fix the relative position of DSSDs and origin of ladder. From now on, we consider factors which had possibilities to have caused the error.

Gaps between linear bushing and shaft

In order to appropriately fix relative position of the jigs, sufficient quality of linear bushings and shafts should be used. As the Fig. 7.6 shows, the gap can be enlarged by the lever arm of structure. In our case, when we glue Origami module and ribs, the height h and d is approximately 90 mm and 30 mm respectively. Therefore, if we required this error to be less than 10 μm, the gap should be less than ~ 3 μm. However, according to an actual measurement with micrometer, the diameter of shaft was smaller by 8 μm. Furthermore, flange perpendicularity is 12 μm[2]. Hence this might have caused translation by 60 μm.

[2]The definition of flange perpendicularity is a tolerance of an internal radius from a vertical axis of flange surface.

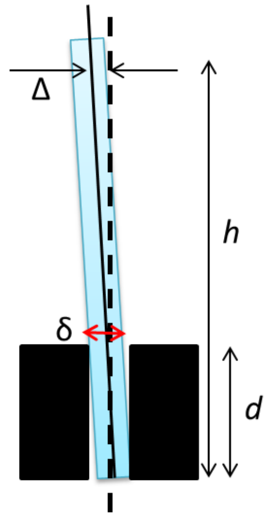

Figure 7.6: Gap of linear bushing is enlarged by lever arm. If the gap of linear bushing between shaft is δ, the gap can be enlarged by $\Delta = \delta \times h/d$.

Gaps between surface of jigs

When we transfered DSSD between two adjacent surface of jigs, more or less movement of DSSD would happened at the moment. According to previous studies, the value was approximately 6 μm per one exchange. In the mockup assembly, dummy aluminum plates were exchanged once. Here, the definition of one exchange is a one-way movement.

Precision of measurement of alignment marks

As mentioned in the last chapter, the precision of measurement of alignment marks is approximately 10 μm.

Conclusion of the consideration

Considering above factors, the error can be $\sim$ 80 μm at a maximum. Although this error is roughly the same order of actual value, it is far from convincing explanation. We must specify the reasons from now on.

7.3 Remaining issues

Aside from the translation or rotation during the ladder assembly, deformation of DSSD and ladder also contribute to degrade the impact parameter resolution. Although it is not possible to correctly evaluate these factors without measuring a real ladder, we can consider them based on an evaluation of the ladder mockups.

7.3.1 Shape of DSSDs

Figure 7.7 shows the surface of n side of DSSD. We just put DSSD on the base of CMM and measured the height. As the plot shows, the n side is concave down and the maximum difference is approximately 20 μm. Other lots of DSSDs had also similar shapes. Although it is preferable to compensate for this shape, it is not simple problem to reflect this information to physics analysis, because there are a lot of chances that surface tension of glue cause deformation. Therefore, we must measure the shape of DSSDs in the state of ladder. It is planned to measure the surface of DSSDs from bottom after assembly.

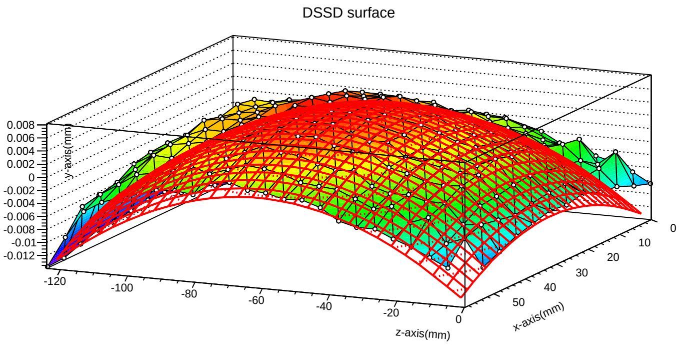

Figure 7.7: Shape of DSSD. Here, the directions of axises are the same as the ladder coordinate system. The vertical position of the origin represents an average of the surface but horizontal position is roughly coincides lower-left corner of DSSD in the Fig. 6.10a. The red mesh is a plot of trial function to which measured points on the surface of DSSD are fit. Though we use Gaussian as the trial function, there are not physical reasoning to use this.

7.3.2 Gravitational sag of the ladder

We must also consider an effect of sag caused by gravity. Because the ladders are mounted with a barrel structure, the direction of gravity differs ladder by ladder. Therefore, we need to evaluate the relation between the magnitude of deformation and direction of gravity. Figure 7.8 shows a situation of sag measurement of layer-6 mockup. We put weight at the center of the ladder and measured the change of height with varying the force. As the graph suggests, deformation could be well approximated by linear function with respect to the applied tension and the gradient was 2.2×10^2 gw/mm. Although this measurement is just substitute for that of real ladders, we were capable to approximate the magnitude of the gravity effect by using density of ladder and achieved value of the coefficient. According to the analysis, the maximum deformation caused by sag was estimated to be approximately 50 μm. This non-negligible magnitude suggests that we need to prepare a formula which represents the deformation by a function of the vector of the gravity. This is a task we have not yet tried.

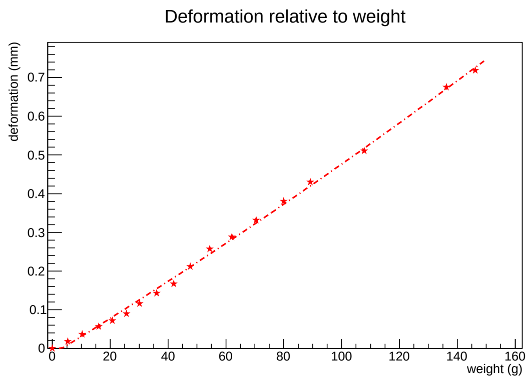

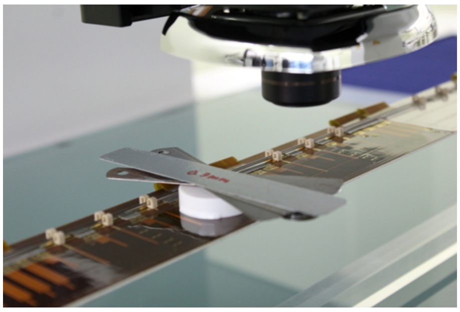

Figure 7.8: Deformation along y axis at the center of layer-6 ladder mockup.

7.3.3 Deformation caused by thermal expansion

We also need to evaluate an expansion of the ladder due to change of temperature. Since the ladder is composed of a lot of materials, it is not possible to get an accurate result without using a numerical technique such as finite element method, but we can roughly evaluate an order of the magnitude. Because coefficient of linear expansion of polyimide, which is a material used for Origami, is known to be ρ_{pol} ~20 ppm/°C [3], the expansion due to change of temperature can be roughly estimated by $L \times \rho_{pol} \times \Delta T$. Here L and ΔT are length of the ladder and change of temperature. If we use $L = 645$ mm as a length of layer-6 ladder, the value becomes 13 μm/°C. We are planning to try a thermal cycling test in order to evaluate this expansion.

[3]This value depends on the kinds of material.

7.4 Future prospects

Considering a start of layer-6 ladders mass production planned from April 2014, the schedule is as follows. First, we must investigate the displacement of DSSD and identify the reasons. Dividing the assembly procedures into small steps and evaluating each factor step by step, we will find solutions for the problems. With the considerations, we could find improvements for jigs such as precision of shaft. Since it is possible to assemble the simplified mockup within a few days and easily evaluate the movement of DSSDs during assembly, it does not take long time to inspect new jigs. Furthermore, if we find a systematic misalignment of DSSDs, we might compensate for the displacement in the initial alignment.

Second, we will make a more realistic ladder with using dummy DSSDs. Here dummy DSSD is not aluminum plate but a mechanical dummy supplied by manufacturing companies. The property of dummy DSSD is the same as real one except their electrical characteristics. Therefore, we can measure much more precisely the movement of DSSDs in a similar procedure as the mass production. Moreover, we will able to evaluate the deformation of DSSDs and the ladder in the final form.

Finally, we will assemble a completely functional ladder, where although bad quality DSSDs and PAs might be used at the beginning, practically usable ladder will be assembled in the same way as the mass production. For that purpose, the procedures should be clarified to everyone who will participate in the mass production by means of the preparation of manual. With this ladder, not only displacement of DSSDs but also yield of bonded wires will be evaluated.

Chapter 8

Conclusion

Towards the start of e^+e^- data taking in Belle II experiment in 2016, we have been developing an assembly procedure of the outermost layer of SVD, which plays a critical role in measuring position of charged particles. The layer is composed of sixteen ladders. We will start their mass production from April 2014.

We have established basic ladder assembly procedure with special jigs. The alignment of DSSDs is performed at the initial stage of the assembly procedures. We set the goal of tolerance of misalignment to be 10 μm from design position. In order to make this alignment easy and effective, we developed a special jig and the assisting software. We have successfully developed the alignment procedure which can be completed within a practical time. For finished ladder, we became able to precisely measure the position of alignment marks.

For an evaluation of the alignment precision of DSSDs in the assembled ladder, we have assembled a mockup with aluminum plates. By comparing the position of scratch marks on aluminum plates, we were able to measure the amount of displacement and found that the horizontal displacement was approximately 100 μm. We have identified some possible sources and will work on additional consideration for a complete explanation and improvement of procedure.

In order to evaluate more realistic parameters, we are planning to assemble a mockup ladder with using mechanical dummy DSSDs whose mechanical characteristics are equivalent to real DSSDs. With this we will be able to evaluate the deformations of components in addition to measurement of displacement of DSSDs.

Towards the start of mass production from April 2014, we will assemble a fully functional ladder with using accepted DSSDs whose strip yield are relatively bad. Here, we will finally evaluate our procedure whether it is ready to tolerate mass production in terms of yield of wires and displacement of DSSDs.

Acknowledgment

I would like to show my greatest appreciation to Prof. Y.Onuki who offered continuing support and constant encouragement. I also would like to thank Prof. T.Higuchi who has offered and managed valuable environment of IPMU where I could grow as a research scientist. With writing the documentation for scholarship as well as this paper, I was received numerous constructive advices from Prof. H.Aihara and Prof. M.Yokoyama. I feel gratitude for them. I would also like to thank people who persistently help me, M. Friedl, K.Hara, C. Irmler, T.Iwashita, R. Kameswara, T.Koga, K.Kono, S.Mineo, J.Sasaki, N.Sato, Y.Seino, Y.Suda, S.Tanaka and T.Tsuboyama.

Bibliography

[1] CKM fitter group main website
http://ckmfitter.in2p3.fr/www/html/ckm_main.html

[2] S. Hashimoto, M. Hazumi, and B. Golob, editors,
Physics at Super B Factory (KEK Report2009-12, 2009),
arXiv:1002.5012[HEP-EX],
http://belle2.kek.jp/physics.html.

[3] P.Raimondi, 2nd SuperB Workshop, Frascati, (2006).

[4] KEK http://www.kek.jp/ja/index.html

[5] Belle II official homepage
http://belle2.kek.jp/

[6] BelleII Technical Design Report
https://belle2.cc.kek.jp/t̃wiki/pub/Organization/B2TDR/B2TDR.pdf

[7] I. Adachi et al. (Belle Collaboration), Phys. Rev. Lett. 108 (2012), 171802.

[8] Belle II Coordinate System and Guideline of Belle II Numbering Scheme

[9] sBelle Design Study Report arXiv:0810.4084 [hep-ex]

[10] M.Firedl et al. Pos VERTEX2011 (2011) 022

[11] The Origami Chip-on-Sensor Concept for Low-Mass Readout of Double-Sided Silicon Detectors
http://www.hephy.at/fileadmin/user_upload/Publikationen/twepp2008_friedl_paper.pdf

[12] APV25-S1 User GuideVersion 2.2

[13] http://www.monotaro.com/

[14] THK website http://www.thk.com/?q=eng/node/202

[15] http://www.tech-jam.com/

[16] http://www.cho-onpa.co.jp/

Appendix A

Belle II detector

We explain the details of Belle II subdetectors.

- beam pipe
  In order to avoid e^+ or e^- colliding atoms of remaining gas in the beam pipe, pressure environment of the beam should be maintained less than $\sim 10^{-8}$ Pa. Beam pipe separates beam and detector regions and enables us to keep a high vacuum. As a requirement for the beam pipe, small radius of the beam pipe is desirable, since vertex detector should be as close to interaction point (IP) as possible. Moreover small amount of material is also required to reduce multiple scattering. Based on this situation, it was decided to use light metal beryllium and inner radius to be only 10 mm. Thanks to stiffness and lightness of beryllium, we succeeded to make it thin to reduce material budget down to $\sim$0.7$\%X_0$.

- PXD
  Pixel detector is the innermost detector which surrounds IP with barrel structure. The layout consists of two layers placed at radii 14 mm and 22 mm from IP and covers full acceptance of Belle II. The purpose of this detector is to precisely measure the decaying point of particles from hit information of daughter particles. In spite of its severe background caused by the upgrade of the accelerator, structure of pixel allows for suppressing an increase of occupancy. Thanks to its fine pitches and lightness, good performance as a vertex detector are achieved: impact parameter resolution $\sigma_z = 25$ μm at 0.5 GeV/c, occupancy 0.5% and material budget 0.38$\%X_0$ in total. By cooperating with SVD, PXD bears a crucial role for reconstruction of vertices.

- SVD
  Si-strip vertex detector is composed of 4 layers, which are allocated

outside PXD at radii from 38 mm to 135 mm from the IP and covers full acceptance of Belle II. Unlike PXD, sensitive areas of SVD are linear shape and allow us to reduce the number of output channels. The role of this detector is supporting PXD to measure the decaying points of particles by teaching the region of interest (ROI). For because of its colossal amount of data, it is impossible to keep all data of PXD. Furthermore, SVD plays a major role in reconstructing K_S vertices. By virtue of ingenuities of readout and large outer volume, sufficient occupancy (10%), impact parameter resolution ($\sigma_z = 30\ \mu$m at 0.5 GeV/c) and reconstruction efficiency of K_S (75%) are accomplished.

- CDC

  Outside SVD central drift chamber is put at radii from 160 mm to 1130 mm. It is able to measure momentum and energy loss dE/dx of charged particles. The information of dE/dx is used for particle identification. Atoms in filled gas (a mixture of He and C_2H_6), are excited by the incident charged particles to produce ions and electrons. These electron-ion pairs are gas-amplified by surrounding electrical field and brought outside. To apply electrical field and read out signals, two kinds of metal wires, called field wire and sense wire, are strained inside CDC. Some sense wires are strained with stereo angle which makes it possible to know z position of particles by measuring the drift time. With the assist of small cell of wires as well as its large volume, CDC can bring out good specification: $\sigma_{p_t}/p_t = \sqrt{(0.2\%p_t)^2 + (0.3\%/\beta)^2}$ and $\sigma_{dE/dx} = 5\%$.

- TOP and ARICH

  Along with CDC, Belle II detector equips two kinds of particle-identification detector, one is Time of propagation counter for barrel part and another aerogel ring-imaging Cherenkov detector for endcap. Main purposes of these detectors are to distinguish charged kaon and pion, where angles of emitted Cherenkov radiation are indirectly measured. Since there is mass difference between kaon and pion, velocities of particles at fixed momenta are not equal. Therefore, by extracting an angle along with the momentum information of CDC, it is capable to guess the species of the incident particle.

  ARICH counter, as the name suggests, measures the ring-image projection. Cherenkov light emitted inside aerogel (synthetic porous derived from a gel replaced with gas) spreads into a circular ring. The angle is measured as a radius of the projected ring. An expected kaon identification efficiency for 1% pion-misidentification probability is greater than 90% within a momentum range from 0.8 GeV/c to 4 GeV/c.

On the other hand, TOP counter measures difference of propagation time inside crystal. When a charged particle enters into large rectangular crystal (2700 mm $\times$ 450 mm $\times$ 20 mm), the emitted Cherenkov light starts to propagates with repeating total reflection and reaches sensor put at both ends. Since the effective distance depends on the angle, propagation time can be converted into the velocity of time. The estimated kaon identification efficiency of TOP counter is >99% for 0.5% probability of misidentification of pion.

- ECL

  Measurement of energy is done by electromagnetic calorimeter. ECL of Belle II is separated into two regions. One is put outside TOP counter at radii from 1250 mm to 1620 mm and another is on endcaps. Both of the detectors are composed of CsI crystals, but in order to reduce scintillation time, any activators are not mixed into endcap crystal. An expected performance of Belle II ECL is $\frac{\sigma_E}{E} = \frac{0.2\%}{E} \oplus \frac{1.6\%}{\sqrt[4]{E}} \oplus 1.2\%$ and $\sigma_{pos} = 5$ mm$/\sqrt{E}$ where E is in GeV.

- KLM

  K_L and muon detector is the outermost detector of Belle II which has roles not only to detect long-lived neutral kaon and muon but also to provide a magnetic field of 1.5 T with superconducting solenoid. As is the case with ECL, it is positioned at barrel and endcap. While the same Resistive Plate Counter (RPC) is mainly used as before, to avoid pileup due to the high luminosity of SuperKEKB, strip scintillator, which has relatively short scintillation time $\sim 10^{-9}$ s, is adopted for inner two layers. Scintillated light inside crystal is lead by fiber into multi pixel photon counter (MPPC). Thanks to good time resolution of scintillator, information about time-of-flight can be used for a determination of momentum of K_L. For 1 GeV/c K_L, an estimated reconstruction efficiency is approximately 80% and momentum resolution is $\sigma_p/p = 18\%$.

Appendix B

Specification of DSSD

Figure B.1 and B.2 are dimensions of large and small rectangle DSSDs which is used for flat part of ladder. Figure B.3 is a dimension of trapezoidal DSSD used for slant part of the ladders. The characteristics of these DSSDs are summarized in Table B.1 and B.2. Here, please note that small and large rectangle DSSDs share same electrical characteristics.

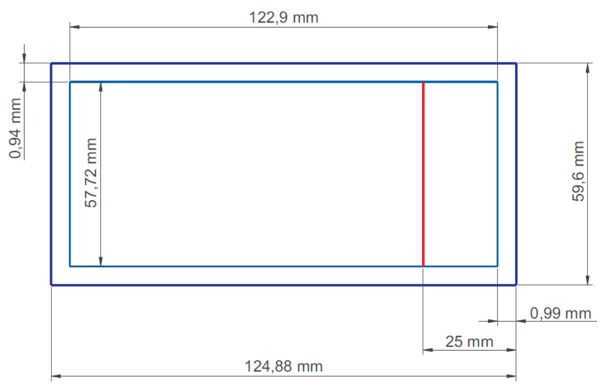

Figure B.1: Geometry of large rectangle DSSD used for layer 4 to layer 6. Red line represents additional bonding pads for PA2. Internal rectangle (light blue line) means sensitive area [6].

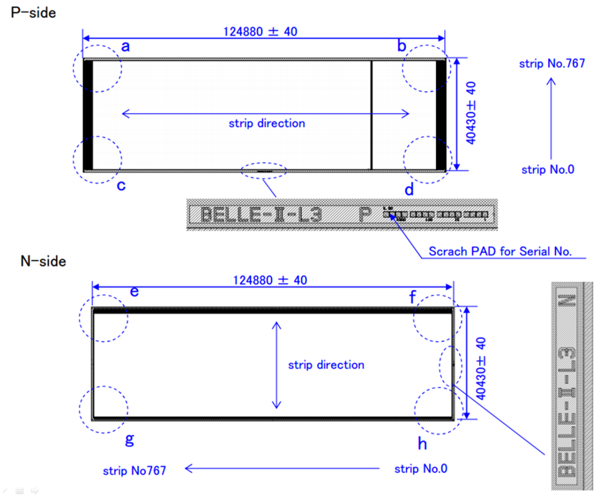

Figure B.2: Geometry of small rectangle DSSD used layer 3 [6].

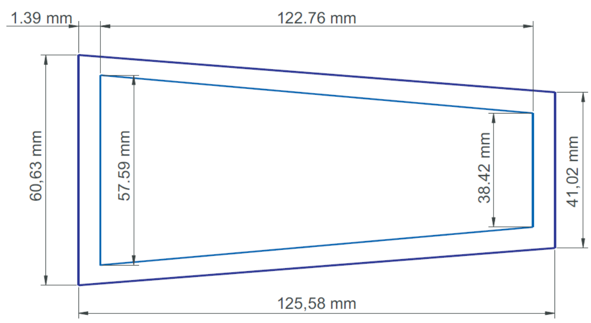

Figure B.3: Geometry of trapezoidal DSSD for slant parts. Internal trapezoidal (light blue line) means sensitive area.

Table B.1: Characteristics of rectangle DSSDs

Quantity	Value
Thickness	320 μm
Strip pitch (z axis)	160 μm (small), 220 μm (large)
Strip pitch ($r\phi$ axis)	50 μm (small), 75 μm (large)
Breakdown reverse voltage (V_r)	200 V
Operation temperature	-20 (min.), 60 (max.)
Base material	Si n-type 8 kΩcm
Full depletion voltage	65 V (min.), 120 V (max.)
PolySilicon resistance (P and N side)	4 MΩ (min.), 10 MΩ (typ.)
Coupling capacitance (P and N side)	100 pF (min.)
Coupling breakdown voltage	20 V (min.)
Bad strip yield	5%
Dark current I_d (V_r=120)	5 μ A
Dark current (V_r=180)	10 μA
Breakdown voltage ($I_d = 10\mu$A)	180 V

Table B.2: Characteristics of trapezoidal DSSD

Quantity	Value
Thickness	300 μm
Full depletion voltage (FD)	40 V (typ.), 70 V (max.)
Base material	Si n-type 8 kΩcm
PolySilicon resistance (P and N side)	10 MΩ (min.), 15 $\pm$ 5 MΩ (typ.)
Breakdown voltage	$>$2.5 $\times$ FD
Interstrip resistance, P side	100 MΩ (min.), 1 GΩ (typ.)
Interstrip resistance, N side	10 MΩ (min.), 100 MΩ (typ.)

Appendix C

Intrinsic resolution of SVD

C.1 Geometrical restrictions

Suppose that a particle passes only one strip like Fig. C.1. For that case, flow of charge comes from only number 1 strip. In principle, therefore, we cannot specify hit position. The resolution is calculated by

$$\sigma_z = \sqrt{\int_{-d/2}^{d/2} z^2 \mathrm{d}z} = \frac{d}{\sqrt{12}}. \tag{C.1}$$

Here d is a width of strip.

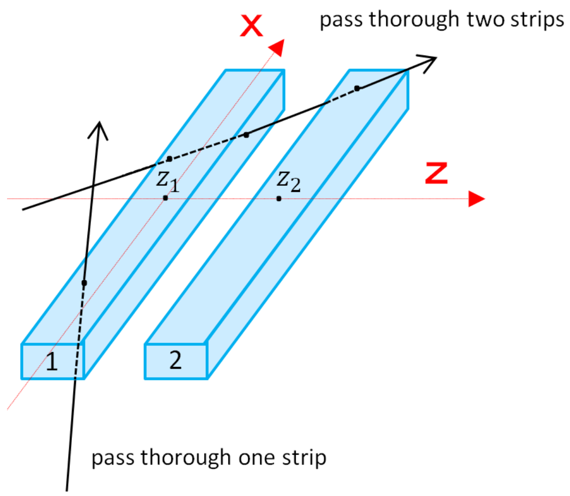

Figure C.1: To make it easy, two strips are drawn. The number in this figure means suffices of strips.

C.2 Center of gravity algorithm

If a particle passes more than two strips, the situation becomes different. Roughly speaking, collected charges would be proportional to distance inside strip. Within a range in which this proportional relation holds, we can calculate the hit position by

$$z = \frac{z_1 q_1 + z_2 q_2}{z_1 + z_2} \tag{C.2}$$

Here z_i and q_i are z component and collected charge of number i strip. If every q_i is dependent each other, we can estimate spatial resolution from Eq.C.2.

$$\sigma_z = \sqrt{\left(\frac{\partial z}{\partial q_1}\right)^2 + \left(\frac{\partial z}{\partial q_2}\right)^2} \cdot \sigma_q \tag{C.3}$$

$$= \frac{\sqrt{q_1^2 + q_2^2}}{(q_1 + q_2)^2} \cdot d \cdot \sigma_q. \tag{C.4}$$

Therefore, resolution of charge, namely, SNR directly restricts intrinsic resolution.

Appendix D

Equipment of layer-6 ladder assembly

D.1 Wire bonder

For layer 6 full ladder assembly, we use automatic rotary head ultrasonic wedge wire bonder, REBO-7W, by Cho-onpa Kogyo, Co. The specifications of this bonder are summarized in Table D.1.

Figure D.1: Automatic wedge bonder REBO-7Ws by Ultrasonic Engineering Co [16].

Table D.1: Specifications of REBO-7Ws

Quantity	Value
Trade name	REBO7W
Wire	25-50 μm
Ultrasonic Frequency	120 kHz
Head movement range	300 $\times$ 160 mm^2
Stroke of height	54 mm
Dimension	80 $\times$ 117 $\times$ 159 cm^3
Power consumption	200V 700VA

D.1.1 Variable parameters of REBO-7Ws

In order to bond wires not only stably but also rapidly, proper tuning of parameters are required. Of all parameters, some determine a deformation of wire, and the others determines a shape of loop.

As for the former parameters, we can give time and power of ultrasonic and force of tool. Meanwhile there are 8 parameters which determine the shape of loops, namely, 2nd-top height, span, loop data, descent timing, cramp timing, table-start timing and Z motion wait. While these names themselves may not be shared with other bonding machines, basic idea is almost same. Optimization of these parameters are main issue of bonding study and even essential for the ladder assembly, but we omit details because of space limitations.

D.2 Coordinate measurement machine

For achieving a given precision, we use coordinate measurement machine (CMM). Fig. D.2 is a picture of CMM. CMM is a measuring instrument which enables us to know 3D position of objects by focusing optically special lens whose depth of field is very small. Almost all of the mechanical QC procedures are done on this machine.

The characteristics are summarized in Table D.2.

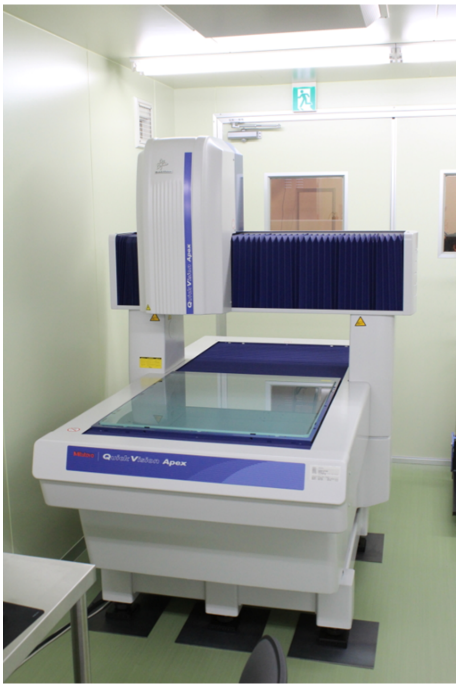

Figure D.2: Picture of coordinate measurement machine.

D.2.1 Coordinate system of CMM

CMM also has its own coordinate. The direction and definition of axis is shown in Fig. D.3. Although it is not impossible to redefine the direction of these axis, it makes difficult to handle controller of CMM.

Table D.2: Specifications of CMM

Quantity	Value
Trade name	QV-H606P1LC (Mitsutoyo Co.)
Code number	363-154
Range (X $\times$ Y $\times$ Z)	600 $\times$ 650 $\times$ 250 mm
Illumination	color LED
Measurement resolution XY	1.5+3L/1000
Measurement resolution Z	1.5+4L/1000
Accuracy-assured temperature	20 $\pm$ 0.3
Load capacity	40 kg

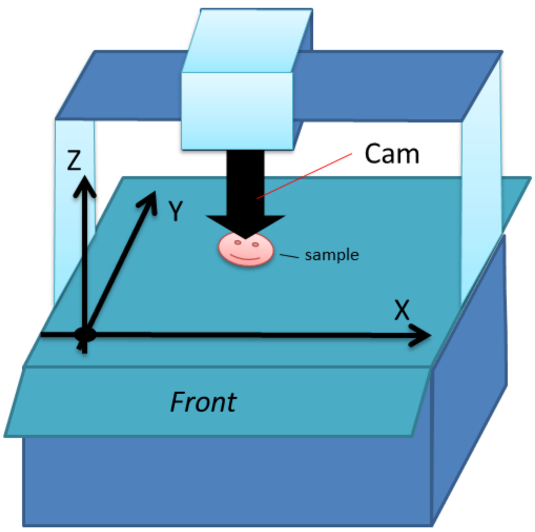

Figure D.3: Definition of machine coordinate system.